

**ISTANBUL TECHNICAL UNIVERSITY ★ GRADUATE SCHOOL OF SCIENCE**  
**ENGINEERING AND TECHNOLOGY**

**EXPERIMENTAL PHASE STUDIES IN THE BaO-CeO<sub>2</sub>-Gd<sub>2</sub>O<sub>3</sub> SYSTEM**



**M.Sc. THESIS**

**Çağrı ÖZTÜRK**

**Department of Metallurgical & Materials Engineering**

**Materials Engineering Programme**

**AUGUST 2017**



**ISTANBUL TECHNICAL UNIVERSITY ★ GRADUATE SCHOOL OF SCIENCE**  
**ENGINEERING AND TECHNOLOGY**

**EXPERIMENTAL PHASE STUDIES IN THE BaO-CeO<sub>2</sub>-Gd<sub>2</sub>O<sub>3</sub> SYSTEM**

**M.Sc. THESIS**

**Çağrı ÖZTÜRK**  
**(506151406)**

**Department of Metallurgical & Materials Engineering**

**Materials Engineering Programme**

**Thesis Advisor: Asst. Prof. Dr. Nuri SOLAK**

**AUGUST 2017**



**ISTANBUL TEKNİK ÜNİVERSİTESİ ★ FEN BİLİMLERİ ENSTİTÜSÜ**

**BaO-CeO<sub>2</sub>-Gd<sub>2</sub>O<sub>3</sub> SİSTEMİNDE DENEYSEL FAZ ÇALIŞMALARI**

**YÜKSEK LİSANS TEZİ**

**Çağrı ÖZTÜRK  
(506151406)**

**Metalurji ve Malzeme Mühendisliği Anabilim Dalı**

**Malzeme Mühendisliği Programı**

**Tez Danışmanı: Yrd. Doç. Dr. Nuri SOLAK**

**AĞUSTOS 2017**









*To my Mom and Dad,*



## **FOREWORD**

I would like to express my thanks to my thesis advisor Asst. Prof. Dr. Nuri SOLAK, for his encouragement, kind support and patience during whole my university life. He always guides me not only in my education life but also in my daily life. Thank you for opening my vision and providing the scientific support but most importantly for believing in me.

I am very thankful to M.Sc. Emin KONDAKÇI (Emin Abi) for his encouragement and support all the time. He was like a brother during whole my education life. I am truly grateful to M.Sc. Rıfat YILMAZ for his expertise and interest.

I would like to present my gratitude to Dr. Ceren YILMAZ AKKAYA and Dr. Barış YAĞCI for their help during XRD and SEM/EDS characterization of samples.

I would like to thank my colleagues, M.Sc. Sena DAYIOĞLUGİL, who always shares her knowledge with me and helps me during my university life, Anıl DEMİRKESEN, Efe YARIŞ, Res. Asst. Gizem SOYDAN, Sinan BOSNA, Fatih KURT and M.Sc. Kübra SADE and Alphan BERKEM.

I would like to thank to Mervan YILDIZ for his kind support and constant encouragement. I cannot end without thanking my parents, Gülay and Bayram, and my sister Ece for their conviction, support and advices. It is to them that I dedicate this work.

August 2017

Çağrı ÖZTÜRK  
(Material Engineer)



## TABLE OF CONTENTS

	<u>Page</u>
<b>FOREWORD</b> .....	<b>ix</b>
<b>TABLE OF CONTENTS</b> .....	<b>xi</b>
<b>ABBREVIATIONS</b> .....	<b>xiii</b>
<b>LIST OF TABLES</b> .....	<b>xv</b>
<b>LIST OF FIGURES</b> .....	<b>xvii</b>
<b>SUMMARY</b> .....	<b>xix</b>
<b>ÖZET</b> .....	<b>xxi</b>
<b>1. INTRODUCTION</b> .....	<b>1</b>
<b>2. FUEL CELL</b> .....	<b>3</b>
2.1 Fuel Cell Types .....	4
2.1.1 Polymer electrolyte fuel cell (PEFC) .....	7
2.1.2 Direct Methanol Fuel Cell (DMFC).....	9
2.1.3 Alkaline Fuel Cell (AFC).....	10
2.1.4 Phosphoric acid fuel cell (PAFC) .....	12
2.1.5 Molten carbonate fuel cell (MCFC).....	13
2.1.6 Solid oxide fuel cells (SOFC) .....	14
<b>3. LITERATURE REVIEW</b> .....	<b>23</b>
<b>4. EXPERIMENTAL STUDIES</b> .....	<b>35</b>
4.1 Powder Preparation .....	35
4.2 Phase Analysis and Characterization .....	43
<b>5. RESULTS AND DISCUSSIONS</b> .....	<b>45</b>
<b>6. CONCLUSION</b> .....	<b>63</b>
<b>REFERENCES</b> .....	<b>65</b>
<b>CURRICULUM VITAE</b> .....	<b>69</b>



## ABBREVIATIONS

<b>AES</b>	: Air Electrode Supported
<b>AFC</b>	: Alkaline Fuel Cell
<b>BCG</b>	: $\text{BaCe}_{0.8}\text{Gd}_{0.2}\text{O}_3$
<b>BCO</b>	: $\text{BaCeO}_3$
<b>CGO</b>	: Cerium-Gadolinium Oxide
<b>CHP</b>	: Combined Heat and Power
<b>DERs</b>	: Distributed Energy Sources
<b>DMFC</b>	: Direct Methanol Fuel Cell
<b>EDS</b>	: Energy Dispersive Spectroscopy Analyses
<b>GDC</b>	: Gadolinium-doped Ceria
<b>JCPDS</b>	: Joint Committee on Powder Diffraction Standards
<b>LCFC</b>	: $\text{La}_{0.6}\text{Ca}_{0.4}\text{Fe}_{0.8}\text{Co}_{0.2}\text{O}_3$
<b>LGSM</b>	: Lanthanum Gallate with Strontium and Magnesium Doped
<b>LSC</b>	: $\text{La}_{0.6}\text{Sr}_{0.4}\text{CoO}_3$
<b>LSCM</b>	: Lanthanum Chromite/Manganite
<b>LSCV</b>	: Strontium and Vanadium Doped Lanthanum Chromate
<b>LSFC</b>	: Lanthanum Ferrite/Cobaltite
<b>LSM</b>	: Lanthanum Manganite
<b>MCFC</b>	: Molten Carbonate Fuel Cell
<b>MIEC</b>	: Mixed Ionic and Electronic Conductor
<b>PAFC</b>	: Phosphoric Acid Fuel Cell
<b>PEFC</b>	: Polymer Electrolyte Fuel Cell
<b>PEMFC</b>	: Proton Exchange Membrane Fuel Cell
<b>SDZ</b>	: Scandium-doped Zirconia
<b>SEM</b>	: Scanning Electron Microscope
<b>SOFC</b>	: Solid Oxide Fuel Cell
<b>XRD</b>	: X-ray Diffraction
<b>YSZ</b>	: Yttrium Stabilized Zirconia



## LIST OF TABLES

	<u>Page</u>
<b>Table 2.1</b> : Main properties of the various fuel cell types.....	5
<b>Table 3.1</b> : Compositions of samples .....	29
<b>Table 4.1</b> : Compositions of samples .....	39





## LIST OF FIGURES

	<u>Page</u>
<b>Figure 2.1</b> : A schematic view of the fuel cell. ....	4
<b>Figure 2.2</b> : A schematic view of planar type stack design.....	6
<b>Figure 2.3</b> : A schematic view of tubular design .....	7
<b>Figure 2.4</b> : A schematic view of polymer exchange fuel cell.....	8
<b>Figure 2.5</b> : A schematic view of alkali fuel cell .....	10
<b>Figure 2.6</b> : Phosphoric acid fuel cell schematic view.....	12
<b>Figure 2.7</b> : Molten carbonate fuel cell schematic view .....	13
<b>Figure 2.8</b> : A schematic view of solid oxide fuel cell .....	15
<b>Figure 2.9</b> : Polarization resistance of CGO added LSFC and LSM .....	17
<b>Figure 2.10</b> : AES cell voltage and current density values for various pressures.....	18
<b>Figure 2.11</b> : Voltage and current density at various temperature .....	19
<b>Figure 2.12</b> : Relationship between temperature, electrical conductivity and electrolyte thickness.....	19
<b>Figure 2.13</b> : Current density and cell voltage change with using pure oxygen (o) and air ( $\Delta$ ) as fuel .....	20
<b>Figure 2.14</b> : Potential and oxygen/carbon ratio values for various H/C ratio .....	20
<b>Figure 3.1</b> : Figure 3.1 Ionic conductivity of $\text{BaCe}_{0.9}\text{Gd}_{0.1}\text{O}_{2.95}$ established into protonic ( $\bullet$ ) and oxide ion ( $\circ$ ) components.....	23
<b>Figure 3.2</b> : Crystal structure of $\text{BaCe}_{0.9}\text{Gd}_{0.1}\text{O}_{2.95}$ .....	24
<b>Figure 3.3</b> : XRD patterns for Ba10CG and BCG15 sintered samples at $1400^{\circ}\text{C}$ ....	25
<b>Figure 3.4</b> : EDS analysis of (a) Ba10CG and (b) BCG15 .....	25
<b>Figure 3.5</b> : XRD patterns of $\text{BaCe}_{1-x}\text{Gd}_x\text{O}_{3-\alpha}$ .....	26
<b>Figure 3.6</b> : Arrhenius plots of the conductivity of $\text{BaCe}_{1-x}\text{Gd}_x\text{O}_{3-\alpha}$ ( $x=0.15, 0.2, 0.25$ ).....	27
<b>Figure 3.7</b> : Water vapor evaluation rate at $600, 800,$ and $1000^{\circ}\text{C}$ .....	27
<b>Figure 3.8</b> : XRD patterns of (a) $1350^{\circ}\text{C}$ , (b) $1500^{\circ}\text{C}$ , (c) $1550^{\circ}\text{C}$ , (d) $1600^{\circ}\text{C}$ and (e) $1650^{\circ}\text{C}$ .....	28
<b>Figure 3.9</b> : XRD of sintered samples.....	29
<b>Figure 3.10</b> : Back Scattered Electron images of (a) Ba10CG, (b) Ba20CG, (c) Ba30CG and (d) Ba40CG.....	30
<b>Figure 3.11</b> : XRD patterns of (a) $\text{Ba}_x\text{Ce}_{0.85}\text{Gd}_{0.15}\text{O}_{3-\delta}$ at $1350^{\circ}\text{C}$ and (b) $\text{Ba}_{1.01}\text{Ce}_{0.85}\text{Gd}_{0.15}\text{O}_{3-\delta}$ after each processing step .....	31
<b>Figure 3.12</b> : SEM image of BCO(Gd) .....	33
<b>Figure 4.1</b> : Conventional solid state technique steps. ....	35
<b>Figure 4.2</b> : Used ball mill in experiment. ....	36
<b>Figure 4.3</b> : Powders view after drying.....	36
<b>Figure 4.4</b> : Calcined powders. ....	37
<b>Figure 4.5</b> : Cold isostatic press. ....	37
<b>Figure 4.6</b> : Sintered pellets. ....	38
<b>Figure 4.7</b> : Sintered pellets (a) $\text{BaCe}_{0.9}\text{Gd}_{0.1}\text{O}_{2.95}$ , (b) $\text{BaCe}_{0.8}\text{Gd}_{0.2}\text{O}_{2.90}$ , (c) $\text{BaCe}_{0.7}\text{Gd}_{0.3}\text{O}_{2.85}$ , and (d) $\text{BaCe}_{0.5}\text{Gd}_{0.5}\text{O}_{2.75}$ .....	38
<b>Figure 4.8</b> : Sol-gel technique steps.....	40

<b>Figure 4.9 :</b> (a) before and (b) after adding chelating agent.....	41
<b>Figure 4.10 :</b> Sample's view after sudden combustion reaction. ....	41
<b>Figure 4.11 :</b> Sample's view after combustion reaction.....	42
<b>Figure 4.12 :</b> (a) before and (b) after calcination step sample's view.....	42
<b>Figure 5.1 :</b> CeO <sub>2</sub> -GdO <sub>1.5</sub> quasi-binary phase diagram. ....	45
<b>Figure 5.2 :</b> BaO-CeO <sub>2</sub> quasi-binary phase diagram.....	46
<b>Figure 5.3 :</b> Quenched and furnace cooled samples of BCG0-67.....	47
<b>Figure 5.4 :</b> Quenched and furnace cooled samples of BCG0-67.....	47
<b>Figure 5.5 :</b> XRD patterns of PBCG0-67 and PQBCG0-67.....	48
<b>Figure 5.6 :</b> BaO-GdO <sub>1.5</sub> quasi binary phase diagram.....	49
<b>Figure 5.7 :</b> Selected sample compositions. ....	49
<b>Figure 5.8 :</b> XRD results of BCG45-5, BCG40-10, BCG35-15 and BCG25-25. ....	50
<b>Figure 5.9 :</b> SEM/EDS results of BCG25-25. ....	51
<b>Figure 5.10 :</b> 48 h and 120 h sintered samples' XRD patterns. ....	51
<b>Figure 5.11 :</b> BCG70-10, BCG50-30, BCG30-50 and BCG10-70 samples' XRD patterns.....	52
<b>Figure 5.12 :</b> SEM/EDS analysis of BCG50-30.....	53
<b>Figure 5.13 :</b> SEM/EDS result of BCG30-50.....	53
<b>Figure 5.14 :</b> A XRD analysis of BCG10-20. ....	54
<b>Figure 5.15 :</b> SEM/EDS results of BCG10-20. ....	55
<b>Figure 5.16 :</b> XRD patterns of BCG10-40 with various sintering time. ....	55
<b>Figure 5.17 :</b> SEM/EDS analysis of BCG10-40.....	56
<b>Figure 5.18 :</b> XRD patterns of 48 h and 120 h sintered samples of BCG10-50.....	56
<b>Figure 5.19 :</b> SEM/EDS analysis of 48 h sintered BCG10-50.....	57
<b>Figure 5.20 :</b> XRD patterns of 48 h and 120 h sintered BCG10-60 samples.....	57
<b>Figure 5.21 :</b> SEM/EDS result of BCG10-60.....	58
<b>Figure 5.22 :</b> Furnace cooled and quenched samples of BCG10-57.....	59
<b>Figure 5.23 :</b> XRD pattern of BCG5-62.....	60
<b>Figure 5.24 :</b> XRD patterns of PBCG25-25 and PQBCG25-25. ....	60
<b>Figure 5.25 :</b> BaO-CeO <sub>2</sub> -GdO <sub>1.5</sub> quasi ternary phase diagram. ....	61

## EXPERIMENTAL PHASE STUDIES IN THE BaO-CeO<sub>2</sub>-Gd<sub>2</sub>O<sub>3</sub> SYSTEM

### SUMMARY

Energy became more important issue with developing technology. Fossil fuels play an important role to produce energy. Nevertheless, they are limiting and environmentally hazardous energy sources. Because of these reasons, energy producers have tended to use renewable energy sources such as hydropower, solar panels, biomass, geothermal energy, and wind turbines. However, there are some disadvantages of these systems; they are transient energy sources and affected so many factors such as wind speed, temperature, ambient, and weather. So they cannot be used in critical applications. At this point, fuel cells are alternative energy sources that are clean, environment-friendly and high efficient systems.

Fuel cells are devices that convert chemical energy directly into electrical energy with high efficiency. In these systems, various types of fuels can be used such as hydrogen, natural gas, carbon monoxide, methane and biomass. Especially, fuel cells use hydrogen as fuel dispose water vapor as waste. This shows fuel cells have zero environmental pollutant emission.

Solid oxide fuel cells are one of the most important members of fuel cells regarding to their high efficiency and operation capability with different types of fuels. However, the main problem of solid oxide fuel cell is that material selection is difficult because of high operating temperature. Thus, various types of materials have been investigated for decreasing operating temperature of solid oxide fuel cells. Gadolinium doped ceria one of the most important material for decreasing operating temperature and increasing efficiency. On the other hand, it has been shown that different dopant addition such as gadolinium, yttrium, europium, lanthanum, and neodymium improved material properties. Gadolinium doped barium cerate is a potential material for fuel cell applications since it works relatively low operating temperature and has high conductivity, high mechanical strength and mixed ion conductivity. Additionally, it has not only oxide ion conductivity but also protonic conductivity thus, it can use all the types of fuels and it has wide application areas.

The purpose of this study is that experimental phase studies in BaO-CeO<sub>2</sub>-GdO<sub>1.5</sub> quasi-ternary system, in which there is no phase diagram data available, at 1300°C with using X-ray diffraction (XRD), scanning electron microscope (SEM) and energy dispersive spectroscopy analyses (EDS).

Various compositions of BaCe<sub>(1-x)</sub>Gd<sub>(x)</sub>O<sub>(3-x/2)</sub> were prepared and they were named according to cerium and gadolinium amount. Conventional solid-state reaction method was used for preparing samples. BaCO<sub>3</sub>, CeO<sub>2</sub> and Gd<sub>2</sub>O<sub>3</sub> were used as starting powders and then they were mixed with alcohol. After that, powders were wet milled and alcohol was disposed from mixture with drying 16h at 150°C. Powders were calcined at 1100°C for 6h and then milled again for reducing particle size. Then powders were pressed at 400 MPa using cold isostatic press. Pellets were sintered at 1300°C for 48h. BCG0-67, BCG0-50 and BCG10-57 samples were

sintered again at 1300°C for 72h for understanding BaGd<sub>2</sub>O<sub>4</sub> phase formation. Moreover, BCG0-67, BCG0-50 and BCG10-57 samples were quenched for examining stability of BaGd<sub>2</sub>O<sub>4</sub> phase.

BCG0-67 and BCG25-25 samples were prepared with the Pechini (sol-gel type wet chemistry) method for crosscheck. In the sol-gel method, Ba(NO<sub>3</sub>)<sub>2</sub>, Ce(NO<sub>3</sub>)<sub>3</sub>.6H<sub>2</sub>O and Gd(NO<sub>3</sub>)<sub>3</sub>.6H<sub>2</sub>O powders were used as starting powders. These powders were mixed with distilled water. They were stirred and heated with magnetic stirrer. During heating one mole citric acid per cation was added as chelating agent, and then a gel formation was observed. When distilled water amount reached below a critical value, a sudden combustion reaction was observed. Then, samples were put into drying oven at 150°C for completing reaction. Organics and water were removed in drying oven and samples formed foam. Then, powders were ground and calcined at 800°C for 6 h. Calcined powders were ground again and pressed at 400 MPa in cold isostatic press thus pellets were produced. Pellets were sintered at 1300°C for 48h. Prepared samples were divided two groups, first of them was cooled in furnace and the second one was quenched. Thus, control experiment of the BaO-CeO<sub>2</sub>-GdO<sub>1.5</sub> quasi-ternary phase diagram was completed. It was determined that BaGd<sub>2</sub>O<sub>4</sub> is high temperature stable phase and it decomposes to BaCO<sub>3</sub> and *b*-type Gd<sub>2</sub>O<sub>3</sub>. Small amount of gadolinium dissolves in barium oxide. Finally, samples were characterized with XRD and SEM/EDS thus quasiternary phase diagram of BaO-CeO<sub>2</sub>-GdO<sub>1.5</sub> was constructed.

## BaO-CeO<sub>2</sub>-Gd<sub>2</sub>O<sub>3</sub> SİSTEMİNDE DENEYSEL FAZ ÇALIŞMALARI

### ÖZET

Enerji yüzyıllardır insanlığın en önemli konularından biri olmuştur. Günümüzde ise gelişen teknoloji ile birlikte enerji daha da önemli bir konu haline gelmiştir. Dünyada kullanılan enerjinin çok büyük bir bölümü fosil yakıtların yakılmasıyla elde edilmektedir. Ancak fosil yakıtların tükenmek üzere olması araştırmaların gelecekte artan enerji ihtiyacını karşılamak için alternatif enerji kaynaklarına odaklanmasını sağlamıştır. Fosil yakıtlar genellikle yakılarak enerji elde edilmekte ve üretilen enerji mekaniksel yöntemlerle elektrik enerjisine dönüştürülmektedir. Mekaniksel enerjinin elektrik enerjisine çevrilmesi kayıplara yol açmakta ve sistemin verimliliğini düşürmektedir. Ayrıca artan enerji talebini karşılamak için bu tip sistemlerin kullanımının yaygınlaşmasıyla doğaya salınan karbon miktarında ciddi bir artış olmuş ve çevre kirliliğini tetiklemiştir.

Günümüzde çevreye zarar vermeyen, temiz, uzun süreli kullanım olanağı sağlayan ve fosil yakıtlara alternatif enerji kaynakları olarak hidro enerji, rüzgar tribünleri, güneş panelleri, jeotermal enerji ve biokütle gibi yenilenebilir enerji kaynaklarının kullanımı daha da yaygınlaşmıştır. Devletlerin bu tip enerji kaynaklarının kullanımını teşvik etmesiyle yenilenebilir enerji kaynaklarından elektrik üretiminin maliyetleri oldukça düşmüş ve kullanımı giderek yaygınlaşmıştır. Ayrıca enerji üretimi sonucunda doğaya salınan karbon miktarı ile ilgili yasal kısıtlamaların getirilmiş olması bu enerji kaynaklarının önemini daha da arttırmıştır. Ancak yenilenebilir enerji kaynaklarının sürekli elektrik üretiminden yoksun olmaları ve hava durumu, sıcaklık, rüzgar hızı, ortam gibi bir çok faktörden etkileniyor olması bu tip enerji kaynaklarının kritik alanlardan kullanımını mümkün kılmamaktadır.

Yakıt pilleri temiz, çevre dostu, sürekli ve yüksek verimlilikle çalışabilen enerji üretim sistemleri olduklarından artan enerji ihtiyacını karşılayacak ve yenilenebilir enerji kaynaklarına alternatif olarak kullanılacak enerji kaynaklarıdır. Günümüzde yakıt pilleri üzerine yapılan çalışmalar giderek artmaktadır. Yakıt pilleri herhangi bir mekaniksel sisteme ihtiyaç duymaksızın kimyasal enerjiyi elektrokimyasal yöntemlerle direkt olarak elektrik enerjisine çevirirler. Mekaniksel sistemler kullanmadıklarından enerji dönüşümü sırasındaki kayıplar en aza indirilmiştir. Yakıt hücreleri yakıt olarak hidrojen, doğal gaz, karbon monoksit, metan ve biokütle kullanabilirler. Özellikle yakıt olarak hidrojen kaynağı kullanan sistemler atık olarak sadece su buharı olduğundan doğaya zarar vermeyen sistemlerdir.

Katı oksit yakıt pilleri yüksek verimlilikleri ve çok çeşitli yakıtlarla çalışabilmeleri nedeniyle yakıt pilleri içinde en fazla önem arz eden yakıt pili çeşididir. Katı yakıt oksit pili porlu yapıdaki katı oksit elektrotlar arasında konumlandırılmış yoğun elektrolit tabakasına sahiptir. Yakıt olarak genellikle hidrojen kullanılmaktadır. Oksijen katot tarafından beslenir ve burada elektronlar vasıtasıyla indirgenerek oksijen iyonları elde edilir. Porlu yapıdaki katot elektrot oksijen gazının ve oksijen iyonlarının taşınmasına izin verecek yapıda iyonik iletkenliğe sahiptir. Ayrıca

reaksiyon sonucu üretilen su buharının geçişine de izin verecek boşluklar içermektedir. Elektrolit tabakası ise moleküler yapıların ve proton iyonlarının geçmesini engelleyen seçici geçirgen yoğun bir tabakadır. Oksijen iyonları elektrolitten geçerek anoda ulaşır ve burada hidrojen gazı ile oksidasyon reaksiyonuna girerek su buharı oluşturur. Reaksiyon sonucunda açığa çıkan elektronlar harici devre vasıtasıyla katoda taşınırlar böylece enerji üretilir. Katoda taşınan elektronlar tekrar oksijen gazının indirgenmesini sağlarlar ve devre tamamlanmış olur. Katı yakıt oksit pilleri yaklaşık 600-1000°C aralığında ve %70 verimle çalışan sistemlerdir. Çalışma sıcaklıklarının yüksek olması sebebiyle birleşik ısı ve güç sistemleriyle entegre edilerek verimlilikleri artırılabilir.

Katı oksit yakıt pillerinde elektrolit olarak genellikle yttria-stabilize zirkonya (YSZ) kullanılmaktadır. Bu malzemenin oksit iyonlarını iletebilmesi için sistem 1000°C sıcaklığına ısıtılmalıdır. Ancak katı yakıt oksit pillerindeki bütün bileşenler bu sıcaklıkta ve ortam koşullarında kararlı olup diğer bileşenlerle kimyasal tepkimeye girmemelidir. Ayrıca mekaniksel özellikleri de bu sıcaklıkta diğer bileşenlerle uyumlu olmalıdır. Bu sıcaklıkta çalışan birbiriyle uyumlu malzemelerin sınırlı olması katı yakıt oksit pillerinin kullanımını kısıtlamaktadır. Araştırmalar katı yakıt oksit pilleri için alternatif malzemelerin bulunmasına ve çalışma sıcaklığının düşürülmesine yoğunlaşmıştır.

Gadolinium doplanmış seryum oksit ve gadolinium, yttrium, evropiyum, lantan, neodyum gibi nadir toprak elementleri doplanmış baryum seryum oksit düşük sıcaklıklarda yüksek iyonik iletkenliğe sahip malzemelerdir. Bu malzemeler hem proton iletkenliği hem de oksit iyon iletkenliğine sahip olmaları sebebiyle tüm yakıtlarla kullanılabilir. Gadolinium doplanmış baryum seryum oksit düşük çalışma sıcaklığı, yüksek iyon iletkenliği ve hem proton hem de oksit iyon iletkenliği özellikleri sayesinde katı oksit yakıt pili uygulamalarında umut vadeden malzemelerden biridir.

Bu çalışmada daha önce literatürde verisi bulunmayan BaO-CeO<sub>2</sub>-GdO<sub>1.5</sub> üçlü faz diyagramının 1300°C sıcaklığı için belirlenmesi amaçlanmıştır. Üçlü faz diyagramının belirlenebilmesi için hazırlanan numunelere X-ışınları spektrometresi (XRD), taramalı elektron mikroskobu (SEM) ve elementel analiz (EDS) teknikleri uygulanmıştır. Analizler sonucunda BaO-CeO<sub>2</sub>-GdO<sub>1.5</sub> üçlü faz diyagramının deneysel olarak tespit edilmesi amaçlanmıştır. Ayrıca üçlü faz diyagramının çizilmesi amacıyla BaO-CeO<sub>2</sub> ve CeO<sub>2</sub>-GdO<sub>1.5</sub> ikili faz diyagramları incelenerek belirlenen sıcaklıklardaki oluşan ara fazlar belirlenmiştir. Ancak BaO-GdO<sub>1.5</sub> ikili faz diyagramı literatürde bulunmadığından hazırlanan numuneler ve uygulanan analiz yöntemleriyle BaO-GdO<sub>1.5</sub> ikili faz diyagramının çizilmesi amaçlanmıştır.

Bu çalışma kapsamında numuneler katı-hal reaksiyonu yöntemiyle hazırlanmıştır. Başlangıç tozu olarak BaCO<sub>3</sub>, CeO<sub>2</sub> ve Gd<sub>2</sub>O<sub>3</sub> kullanılmıştır. Belirlenen kompozisyonlarda hazırlanan numuneler alkol ile karıştırılarak bilyalı öğütücüde 6 saat ve 300 rpm hızda öğütülerek tane boyutu küçültülmüştür. Daha sonra elde edilen numuneler 16 saat 150°C sıcaklıkta tutularak alkol uçurulmuştur. Elde edilen tozlar 1100°C sıcaklıkta 6 saat süreyle kalsine edilmiştir. Kalsine edilen tozlar tekrar bilyalı öğütücüde 30 dakika 300 rpm hızda öğütülmüştür. Öğütülen tozlar silikon kalıplara doldurularak 400 MPa basınç altında soğuk izostatik pres kullanılarak preslenmiş ve pelet elde edilmiştir. Elde edilen peletler 1300°C sıcaklıkta açık atmosferde 48 saat sinterlenmiş ve böylece nihai ürün elde edilmiştir. Numunelerin isimlendirilmesi içerisinde bulunan seryum ve gadolinium miktarına göre yapılmıştır. Örneğin

BCG25-25 bileşiminde %25 seryum, %25 gadolinyum bulunmaktadır geri kalan miktar ise her zaman baryum olmaktadır.

Hazırlanan BCG0-67, BCG0-50 ve BCG10-57 numuneleri hızlı soğutularak ve ayrıca ekstra 72 saat 1300°C sıcaklıkta ısıl işleme tabi tutularak BaGd<sub>2</sub>O<sub>4</sub> fazının kararlı olup olmadığı araştırılmıştır. Ayrıca BCG0-67 ve BCG0-50 numuneleri sol-gel metoduyla hazırlanarak katı hal reaksiyonu tekniğiyle hazırlanan aynı kompozisyondaki numuneler arasında fark olup olmadığı incelenmiştir. Sol-gel yönteminde başlangıç tuzları olarak Ba(NO<sub>3</sub>)<sub>2</sub>, Ce(NO<sub>3</sub>)<sub>3</sub>.6H<sub>2</sub>O ve Gd(NO<sub>3</sub>)<sub>3</sub>.6H<sub>2</sub>O kullanılmıştır. Tuzlar saf su içinde ısıtıcı karıştırıcıda çözülmüştür. Karıştırma esnasında belirli aralıklarla şelat yapıcı olarak katyon başına bir mol sitrik asit ilave edilmiştir. Böylece metal iyonları ile sitrik asit arasında organik bağ oluşturularak çözeltinin jelleşmesi sağlanmıştır. Çözeltideki su uzaklaştırılarak ani yanma reaksiyonu gerçekleşmiştir. Ani yanma reaksiyonu bileşiklerin ön oluşum aşamasıdır ve bu aşamadan sonra numuneler etüve konarak reaksiyonun devam etmesi sağlanmıştır. Etüvdeki numuneler içerisindeki organikler ve suyun uzaklaşması sonucu kabarmıştır, böylece reaksiyon tamamlanmıştır. Daha sonra numuneler öğütülerek krozelere konmuş ve 800°C sıcaklıkta 6 saat süreyle kalsinasyon işlemi gerçekleştirilmiştir. Kalsinasyondan çıkan tozlar öğütülerek 400 MPa basınç altında soğuk izostatik preste preslenmiş ve pelet oluşturulmuştur. Oluşturulan peletler 1300°C sıcaklıkta 48 saat süreyle sinterlenmiştir. Hazırlanan numuneler hem hızlı soğutularak hem de fırın içinde soğutularak fazlar incelenmiştir. Katı hal reaksiyonu ve sol-gel yöntemiyle üretilen numunelerin XRD ve SEM/EDS analizleri sonucunda elde edilen veriler kullanılarak BaO-CeO<sub>2</sub>-GdO<sub>1.5</sub> üçlü faz diyagramı ve BaO-GdO<sub>1.5</sub> ikili faz diyagramı çizilmiştir.

Bu araştırmanın sonucunda BaGd<sub>2</sub>O<sub>4</sub> yüksek sıcaklık fazı olduğu tespit edilmiş, bu fazın düşük sıcaklıklarda BaCO<sub>3</sub> ve monoklinik Gd<sub>2</sub>O<sub>3</sub> fazlarına parçalandığı tespit edilmiştir. Ayrıca baryum seryum oksit katı eriyik formundaki fazda, gadolinyum oksit miktarı arttıkça malzemenin mekanik direnci düşmekte ve çatlak oluşmaktadır. Çalışmanın diğer bir sonucu ise gadolinyumun baryum içinde bir miktar çözüldüğü tespit edilmiştir.



## 1. INTRODUCTION

Energy has been one of the important topics of humanity through ages. The large part of the world energy demand is met by fossil fuels. However, main concern is that fossil fuels are limited sources and they cause environmental pollution. Thus, researchers focus on alternative renewable energy sources such as solar, wind, geothermal and hydropower. Nevertheless, these power sources are transient energy sources and affected so many factors such as wind speed, temperature, ambient, and weather. So they can not be used in critical applications. Fuel cells are alternative energy sources due to the fact that they are clean, environmental-friendly, sustainable and high efficiency power sources.

Fuel cells are devices that convert chemical energy directly into electrical energy with high efficiency. In these systems, various types of fuels can be used such as hydrogen, natural gas, carbon monoxide, methane and biomass. Especially fuel cells that are used hydrogen as fuel dispose water vapor as waste. This shows fuel cells have zero environmental pollutant emission [1], [2].

Solid oxide fuel cells are one of the most important member of fuel cells due to their high efficiency and capability of operating with different types of fuels. However, the main problem of solid oxide fuel cell is that material selection is difficult because of high operating temperature. Yttria-stabilize Zirconia (YSZ) is the most used electrolyte material of solid oxide fuel cell. This material has high ionic conductivity at 1000°C, thus it has to be heated. Electrolyte should be compatible with other cell components thus suitable anode and cathode material selection with YSZ is not only expensive but also very limited. As a result of these disadvantages, researches have been focused on reducing operating temperature of solid oxide fuel cells, to decrease material cost [3].

Some of the studies indicated that gadolinium doped ceria or barium cerate with various dopant such as gadolinium, yttrium, europium, lanthanum, and neodymium has great potential for decreasing operating temperature of solid oxide fuel cells [4].

Gadolinium doped barium cerate [Ba(Ce,Gd)O<sub>3</sub>] is one of the recent developed electrolyte material, which has high oxide-ionic and proton conductivity at, lower temperatures. In addition, it has higher conductivity than other doped cerates. All types of fuel can used in the doped cerate due to mixed ionic conductivity property thus this material become more important. Moreover, it operates between 400-1000°C.

In this thesis, it was aimed to determine the BaO-CeO<sub>2</sub>-GdO<sub>1.5</sub> quasi ternary phase diagram at 1300°C by using various characterization methods such as XRD and SEM/EDS. The used synthesis methods are conventional solid state reaction and sol-gel method; furthermore, in the framework of the thesis study, for the first time in literature BaO-CeO<sub>2</sub>-GdO<sub>1.5</sub> quasi ternary phase diagram and BaO-GdO<sub>1.5</sub> quasi-binary phase diagram were constructed.

## 2. FUEL CELL

Fuel cells are devices that convert chemical energy directly into electrical energy with using electrochemical reactions; reduction and oxidation. Fuel cell consists two electrodes, anode and cathode, these electrodes are separated from each other with an electrolyte to ensure ionic conduction for oxidation reaction [1], [5]–[7].

Classical power generators produce energy by using mechanical parts and this causes losses and decreasing efficiency. On the other hand, fuel cells generate energy directly by electrochemical reaction rather than classical power generators so losses are eliminated in these systems. Thus, they have higher efficiency than classical systems. Fuel cells are environmentally friendly systems since combustion reaction does not occur as in conventional energy generation systems [8].

The first hydrogen-oxygen fuel cell was demonstrated by William Groove in 1839 [9]. In the experiment performed by Groove, water was electrolyzed to hydrogen and oxygen with using a power supply and platinum electrodes, then power supply was removed from system and replaced with an ammeter, a small current flow was detected on the ammeter due to movement of electrons from the anode to the cathode through an external circuit [10], [11]. Francis T. Bacon had produced first 6 kW alkaline fuel cell in 1950s [12]. In 1960s, first polymer electrolyte membrane fuel cells were produced by General Electric and used in Gemini, which was US Space program. Since then researchers focused on development of fuel cells owing to their high efficiency and environment friendly electric production property.

A typically fuel cell contains porous anode and cathode layers and a dense electrolyte which is compacted between these two layers. Figure 2.1 represents a schematic view of the typical fuel cell with ion transport, fuel, oxidant, and gas flows through the cell. In typical fuel cell, fuel (hydrogen, carbon monoxide, methane, methanol, ethanol, etc.) is continuously fed by the anode side and oxidant (oxygen) is fed by the cathode side. Oxygen ions move through the electrolyte from anode to cathode and they react with the fuel on the cathode surface. The electrons, which are emitted as product of the oxidation reaction on the cathode surface, move through the opposite

direction of ion motion and they are carried to the cathode by the external circuit [6], [13]. These electrons reduce oxygen and form new oxygen ions, thus continuous electricity production is provided. The water, which is one of the products of oxidation reaction, is removed from the system.

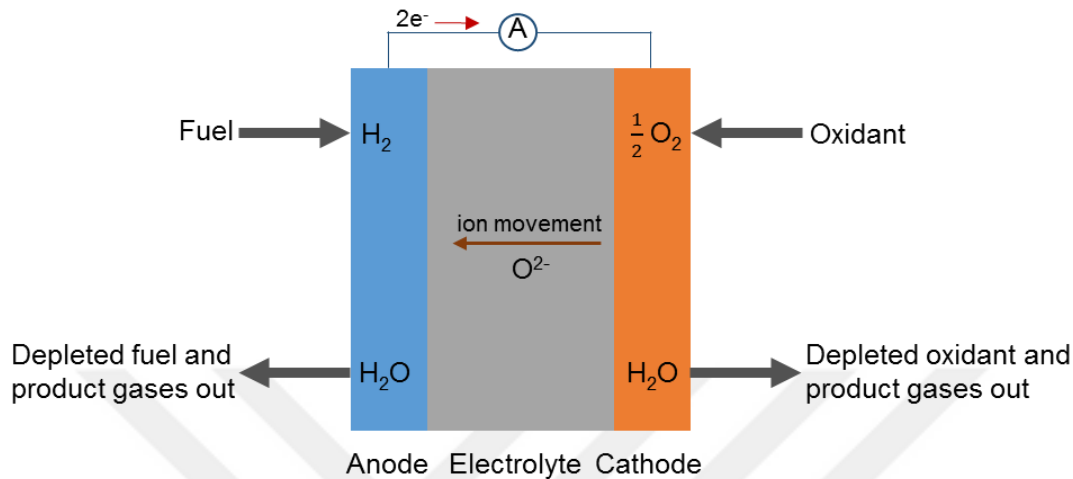


**Figure 2.1 :** A schematic view of the fuel cell.

The electrolyte has to be high ionic conductive and zero electron conductive material; furthermore, it should transport ions, which are produced from fuel, between electrodes. Electrolyte form barrier for preventing direct contact of fuel and oxidant gas stream because of that if fuel (hydrogen) and oxidant (oxygen) interact directly with each other, this causes the explosion. Electrodes have both ionic and electrical conductivity to allow ion transfer for electrochemical reaction and electron transport from the external circuit. The porous electrodes homogeneously distribute reactant gases to the cell and allow removing the reaction products from the cell. In addition, anode, electrolyte, and cathode materials have to be chemical stability and compatibility with each other due to the reactions taking place in the anode and the cathode.

## 2.1 Fuel Cell Types

Fuel cells are usually classified according to the used electrolyte type such as Polymer Electrolyte Fuel Cell (PEFC), Direct Methanol Fuel Cell (DMFC), Alkaline Fuel Cell (AFC), Phosphoric Acid Fuel Cell (PAFC), Molten Carbonate Fuel Cell (MCFC) and Solid Oxide Fuel Cell (SOFC). Table 2.1 shows specifications of various fuel cells[2], [6], [14].

**Table 2.1** : Main properties of the various fuel cell types [2], [6], [14].

	Electrolyte	Electrodes	Catalyst	Interconnect	Operating temperature	Charge carrier	Anode reaction	Cathode reaction
PEFC	Hydrated polymeric ion exchange membranes	Carbon	Platinum	Carbon or metal	40-80°C	H <sup>+</sup>	H <sub>2</sub> → 2H <sup>+</sup> + 2e <sup>-</sup>	O <sub>2</sub> + 4H <sup>+</sup> → 2H <sub>2</sub> O
DMFC	Polymer membranes	Platinum-ruthenium supported carbon and platinum supported carbon	Platinum	Graphite	50-120°C	H <sup>+</sup>	CH <sub>3</sub> OH + H <sub>2</sub> O → CO <sub>2</sub> + 6H <sup>+</sup> + 6e <sup>-</sup>	$\frac{3}{2}$ O <sub>2</sub> + 6H <sup>+</sup> + 6e <sup>-</sup> → 3H <sub>2</sub> O
AFC	Mobilized or immobilized potassium hydroxide in asbestos matrix	Transition metals	Platinum	Metal	65-220°C	OH <sup>-</sup>	H <sub>2</sub> + 2OH <sup>-</sup> → 2H <sub>2</sub> O + 2e <sup>-</sup>	O <sub>2</sub> + 2H <sub>2</sub> O + 4e <sup>-</sup> → 4OH <sup>-</sup>
PAFC	Immobilized liquid phosphoric acid in SiC	Carbon	Platinum	Graphite	160-220°C	H <sup>+</sup>	H <sub>2</sub> → 2H <sup>+</sup> + 2e <sup>-</sup>	O <sub>2</sub> + 4H <sup>+</sup> + 4e <sup>-</sup> → 2H <sub>2</sub> O
MCFC	Immobilized liquid molten carbonate in LiAlO <sub>2</sub>	Nickel and Nickel oxide	Electrode material	Stainless steel or Nickel	650°C	CO <sub>3</sub> <sup>2-</sup>	H <sub>2</sub> + CO <sub>3</sub> <sup>2-</sup> → H <sub>2</sub> O + CO <sub>2</sub> + 2e <sup>-</sup>	O <sub>2</sub> + 2CO <sub>2</sub> + 4e <sup>-</sup> → CO <sub>3</sub> <sup>2-</sup>
SOFC	Perovskite oxides	Perovskite and Perovskite/metal cermet	Electrode material	Nickel, ceramic, or steel	600-1000°C	O <sup>2-</sup>	H <sub>2</sub> + O <sup>2-</sup> → H <sub>2</sub> O + 2e <sup>-</sup>	CO + O <sub>2</sub> → CO <sub>2</sub> + 2e <sup>-</sup>

Fuel cells are also classified according to their operating temperatures as low temperature, intermediate temperature, and high temperature fuel cells and using fuels type as solid fuels (coke), liquid fuels (alcohol, hydrocarbons), and gas fuels (hydrogen, air, oxygen, ammonium, methanol).

Fuel cells are combined each other to form a stack, since a single fuel cell can not produces enough energy. Generally, fuel cells are connected to each other in a series using electrically conductive interconnects. There are two different stacks: planar and tubular stacking.

Planar stacking is the most used fuel cell stack design. Figure 2.2 represents a schematic view of planar type fuel cell stack design. Interconnects, which are located between electrodes, provide electrical conductivity between cells, distribute the reactant gases owing to channeled structure and serve as a barrier for prevent to mix inlet and outlet gases with each other [1]. Planar stack design has a more compact structure than tubular stack design, but gas-tight sealing is necessary.

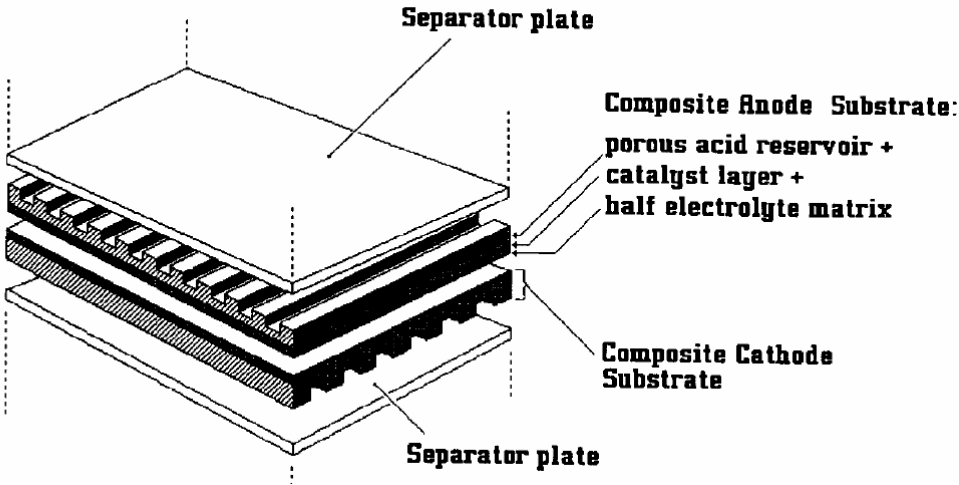


**Figure 2.2 :** A schematic view of planar type stack design [1].

Depending on the gas flow, planar stacks can be divided into five different groups, which are cross-flow, co-flow, counter-flow, serpentine flow, and spiral flow. In cross-flow, gas and fuel flow are perpendicular to each other, in co-flow, fuel and air flow are parallel to each other, in counter-flow, fuel and air flow are in parallel but in opposite directions, in serpentine flow, air follow zig-zag path, and spiral flow are used in circular cells.

Tubular stack is preferred especially for fuel cells which operating at high temperatures. Sealing is not a constraint in tubular design, it is an advantage compared to the planar design. In addition, problems that may arise due to the fact that thermal expansion in high temperature can be eliminated in this design and structural integrity is ensured. Figure 2.3 presents a schematic view of tubular stack. According to this design, air-feed tube is wrapped with cathode, electrolyte and anode; moreover, the interconnect is located at outer surface of the tube [1], [15].

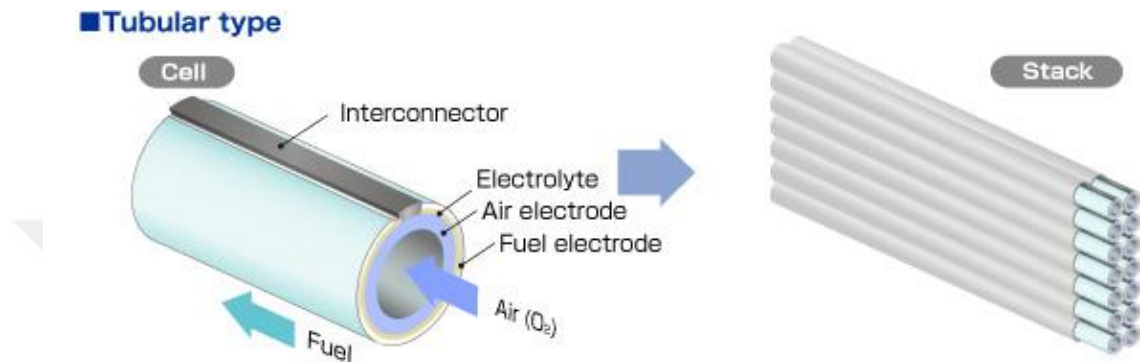


**Figure 2.3 :** A schematic view of tubular design [66].

### 2.1.1 Polymer electrolyte fuel cell (PEFC)

Polymer Electrolyte Fuel Cell (PEFC) is also known as Proton Exchange Membrane Fuel Cell (PEMFC). In this type of fuel cell, the mobile ion is  $H^+$  and proton movement is observed in the solid electrolyte, so the proton exchange membrane (fluorinated sulfonic acid polymer or other similar polymer) is used. This type of membrane has high protonic conductivity and zero electron conductivity [1], [12]. Water is formed at the cathode side as a result of electrochemical reaction and it is the only liquid phase in cell, so the corrosion problem is eliminated. Carbon electrodes are used with platinum or palladium catalyst. Furthermore, carbon or metal is used as an interconnect material. PEFC has a very high power density, low cost, and low operating temperature compared to other fuel cells [16]. Figure 2.4 represents a schematic view of typical polymer exchange fuel cell.

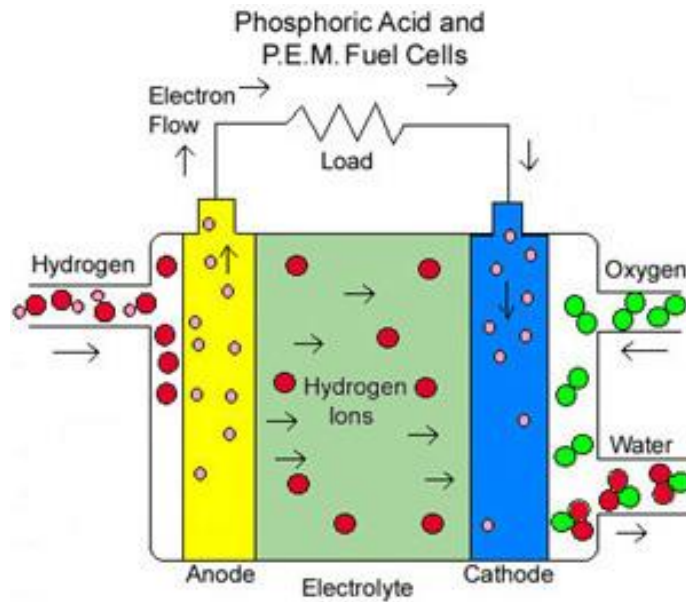


**Figure 2.4 :** A schematic view of polymer exchange fuel cell [17].

Anode, cathode and overall reactions in PEFC systems are shown in equations 2.1, 2.2 and 2.3. These systems usually use hydrogen as fuel.



The basic feature of this membrane, which is usually Nafion, is that it has a structure that allows the movement of protons and blocks the movement of electrons and oxide ions. Generally, planar stack is used in this type of fuel cells.  $\text{H}^+$  ions move through vacancies in the structure. Ion movement depends on bonds and free water association. Water balance is crucial for PEFC because of electrolyte has high ionic conductivity when the cell had high water content [18]. Thus membrane must be hydrated for efficient transport of protons. Therefore, by-product water does not evaporate faster than it produced. Operating temperature and oxygen pressure are other parameters that affect the performance of fuel cell. PEFC operating temperature less than  $100^\circ\text{C}$ , generally  $60\text{-}80^\circ\text{C}$  for providing water balance. When operating temperature increases, ohmic resistance decreases thus cell efficiency increases. When the oxygen pressure increases, the cell voltage increases.

PEFC is one of the main power sources used especially in cars and light trucks. In these systems, hydrogen, methanol and gasoline are used as a fuel. It is used in

vehicle systems due to lightweight and high current density. Another application of PEFC is stationary power plants. Despite increasing the amount of energy produced by forming stack, still PEFC has very low energy production capacity. PEFC energy generator capacity varies between 1 to 10 kW. Natural gas or propane is used as fuel in this system[14].

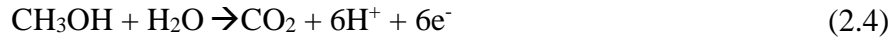
Advantages of PEFC are that resistance to gas crossover since solid electrolyte is present, short start-up time due to low operating temperature, higher current density (4 amps/cm<sup>2</sup>) than others (1 amps/cm<sup>2</sup>), hydrogen fuel usage, and rapid response to load change [19].

Disadvantages of PEFC are that thermal management and using with integrated combustion units are difficult due to the low operating temperature, electrolyte hydration has to be controlled for achieving high efficiency, and it is very sensitive to catalyst poisoning and other contaminants[1].

### **2.1.2 Direct Methanol Fuel Cell (DMFC)**

Working principle of Direct Methanol Fuel Cell (DMFC) is very similar with PEMFC. It uses a special type of polymer electrolyte (Nafion), platinum-ruthenium supported on carbon anode and platinum supported carbon cathode [20]. In DMFC, methanol and water mixture is fed by anode side and oxygen is fed by cathode side. These ingredients react electrochemically each other on anode and form protons, electrons and CO<sub>2</sub> as products. Then protons move to cathode through semipermeable electrolyte, thus water is produced as a result of protons and oxygen reaction. Electrons, which are formed in consequence of these reactions, generate energy by transporting through external grid. DMFC works between 50-120°C and uses H<sup>+</sup> as charge carrier[21]. Generally, DMFC is used in vehicles and portable electronic devices.

Anode, cathode and overall reactions are shown in equations 2.4, 2.5 and 2.6 [22], [23].



Main advantages of DMFC are that it has compact size, high energy density, used fuel can be stored easily, and simple thermal management because of low operating temperature. On the other hand, disadvantages of DMFC are that it has low cell voltage and efficiency, fuel and water crossover, high cost, fuel toxicity, complex water management [24].

### 2.1.3 Alkaline Fuel Cell (AFC)

Alkaline Fuel Cell (AFC) is one of the first developed fuel cell technologies and is used to meet the on-board electricity and water needs of spaceships. This fuel cell is similar with PEFC, but the main difference between them is that AFC uses alkali membrane instead of acid membrane; furthermore, AFC uses  $\text{OH}^-$  ions as mobile ions but in PEFC,  $\text{H}^+$  ions are mobile. In AFC, potassium hydroxide (KOH) aqueous solution is used as an electrolyte [25]. AFC systems operate between 120-250°C and the main factor determining the operating temperature is the amount of KOH solution in the electrolyte. Operating temperature increases with increasing KOH concentration in aqueous solution.

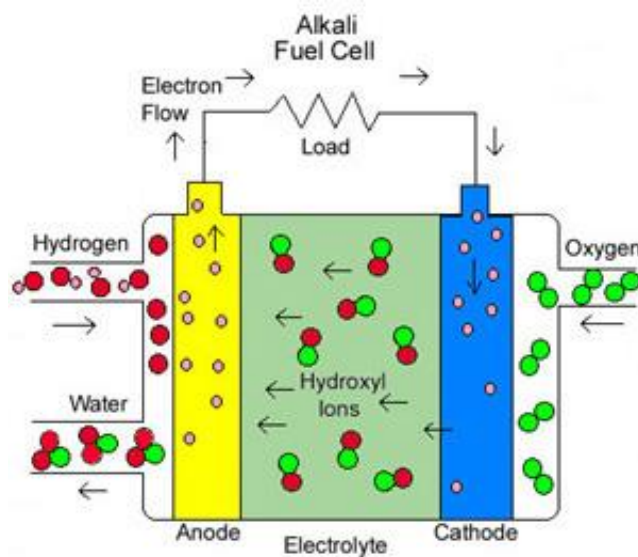


**Figure 2.5** : A schematic view of alkali fuel cell [17].

Figure 2.5 shows a schematic view of an alkaline fuel cell. Hydrogen is used as fuel and electricity is produced by the external circuit, which consists the electrons that are released after the oxidation of hydrogen. Anode, cathode and overall reactions are shown in equations 2.7, 2.8 and 2.9.



The hydroxyl ions, which are formed by electrochemical reaction in the cathode side, move to the anode side. On the anode surface, it reacts with hydrogen and generates water. Released electrons, which are products of this reaction, produce energy. Mobilized or immobilized potassium hydroxide in asbestos matrix is used as an electrolyte in AFC. Platinum is used as catalyst and transition metals are used as electrode.

The cell performance improves with increasing pressure and temperature. Increasing temperature reduces activation polarization, mass transfer polarization and ohmic losses.

Main advantages of AFC are that it provides better efficiency and higher performance than other types of fuel cells when they are fed with hydrogen and oxygen; moreover, it has quick start property[26].

On the other hand, main disadvantage of this system is the presence of  $\text{CO}_2$  in the system which reduces cell performance because of that it combines with hydroxide to form carbonate. This reaction is shown in equation 2.10 [27].



As a result of this reaction, hydroxide concentration decreases and the electrolyte viscosity increases which causes a lower diffusion rate and limiting current. Liquid electrolyte usage causes wettability and corrosion problems.

### 2.1.4 Phosphoric acid fuel cell (PAFC)

Phosphoric Acid Fuel Cell (PAFC) was the first commercialized and first generation of modern fuel cell and this type of fuel cell used extensively due to the high capacities. PAFC usually operates at a working temperature of 150-220°C [22]. It uses liquid phosphoric acid (H<sub>3</sub>PO<sub>4</sub>) as electrolyte. Silicon carbide membrane and Pt catalysts are used in these systems. Figure 2.6 shows a schematic view of PAFC.

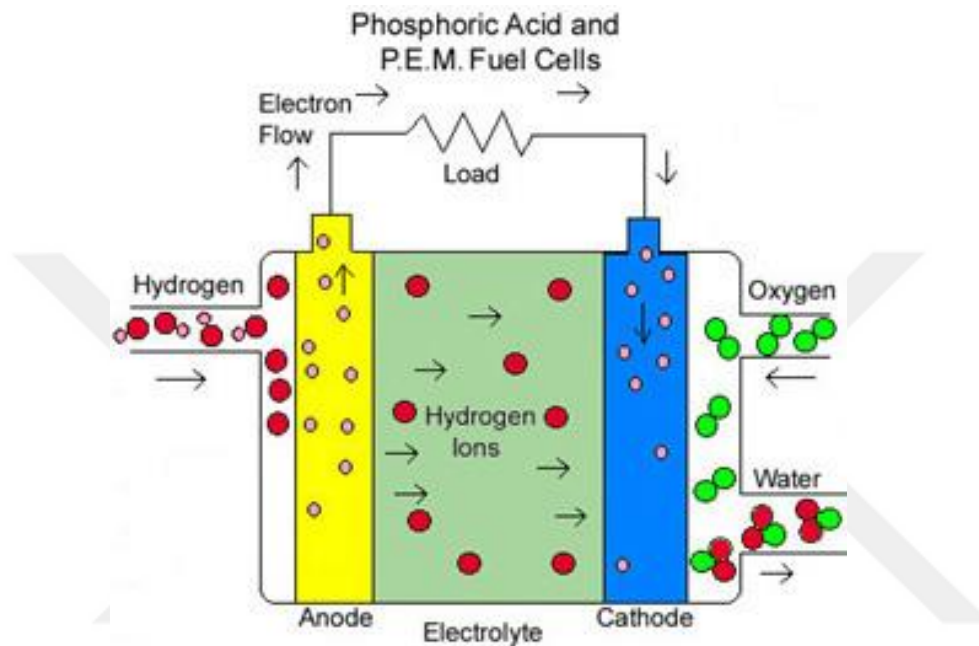


**Figure 2.6** : Phosphoric acid fuel cell schematic view [17].

The operation of these cells is similar to the working mechanism of PEFC and mobile ion in these cells is H<sup>+</sup>. Anode, cathode and overall reactions are given in equations 2.11-2.13.



PAFC performance is affected by pressure, temperature, reactant gas composition, fuel utilization and impurities (from fuel and oxidant gases). Cell performance increases with increasing pressure. Generally, it is used in stationary power generations and heavy vehicles such as busses and trucks.

The main advantages of PAFC systems are that they are less sensitive to CO<sub>2</sub> compared to PEFC and AFC. Since the working temperature is still low, there is no

difficulty in material selection. System efficiency is higher than PEFC. Furthermore, efficiency can be further increased by Combined Heat and Power (CHP) system [21]. Disadvantages of the PAFC are that the oxygen reduction at the cathode side is slower than AFC and it is necessary that use Pt catalyst; moreover, material selection is important and leads to cost because phosphoric acid is highly corrosive.

### 2.1.5 Molten carbonate fuel cell (MCFC)

Molten Carbonate Fuel Cell (MCFC) operates at about 650°C. In these systems, the mobile ion is  $\text{CO}_3^{2-}$  and a mixture of hydrogen and  $\text{CO}_2$  is used as fuel [28]. In this system, Ni-based alloys anode, Ni-oxide cathode and molten alkali carbonate salts electrolyte are used [29]. The schematic view of MFCF is shown in Figure 2.7.

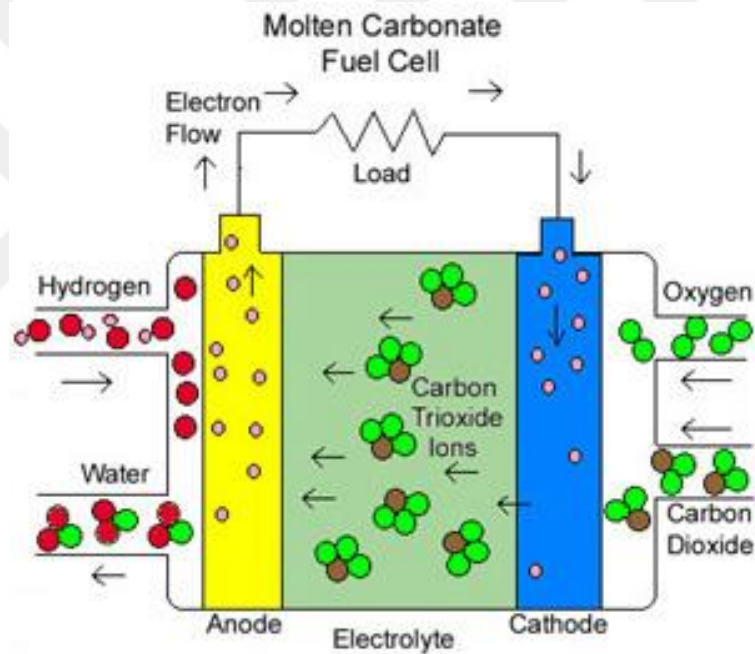


**Figure 2.7 :** Molten carbonate fuel cell schematic view [17].

$\text{CO}_3^{2-}$  ions pass through the molten electrolyte and generate  $\text{CO}_2$  and water that is by-product of the oxidation reaction of hydrogen and  $\text{CO}_3^{2-}$  ions in the anode side.  $\text{CO}_2$  is removed from anode side and fed to cathode side which results in formation of  $\text{CO}_3^{2-}$  ions. Equations 2.14-2.16 show anode, cathode and overall reactions [30].



MCFC has higher efficiency than PAFC since MCFC operates at high temperature. However, it has higher risk of corrosion due to molten carbonate electrolyte and it has shorter lifetime. Generally, it is used in stationary power plants and marine applications.

Pressure, temperature, gas composition and gas utilization factors affect the performance of the cell. Performance of the cell increases with increasing pressure which causes increase in the partial pressure of the reactant, gas solubility, and mass transport rate. However, some undesirable reactions occur in the anode and cathode at high pressure. According to the Boudard reaction, carbon deposition and methane formation are observed in the cell. Carbon deposition causes plugging gas passage of anode side. Methane formation leads to reduce cell performance and reactant's loss because of that per mole methane reacts with three moles hydrogen [31]. According to this reaction, hydrogens are consumed thus gas composition balance is disordered. Cell performance increases with increasing temperature until 650°C. After this temperature efficiency of MCFC decreases with increasing temperature because of that electrolyte loss from evaporation and increased corrosion.

Advantages of MCFC are that it has high efficiency, can be combined with CHP, is not affected by carbon monoxide and does not need noble metal for oxidation and reduction reactions because of that it operates at high temperature [32]. Besides, it is highly sensitive to sulphur and it has slow start-up time.

### **2.1.6 Solid oxide fuel cells (SOFC)**

Solid oxide fuel cells (SOFCs) operate at high temperatures using solid-phase metal oxide and ceramic materials that convert chemical energy directly into electrical energy. When combined with cogeneration and trigeneration systems due to the high operating temperature of the SOFC, it operates at a higher efficiency (70%) than conventional techniques and other fuel cells. The SOFC operates at temperature range of 600-1000°C [33]. It has three basic compounds that are porous anode (typically Ni-ZrO<sub>2</sub> cermet or Co-ZrO<sub>2</sub>) and cathode (typically Sr-doped LaMnO<sub>3</sub>) and dense electrolyte (usually yttrium stabilized zirconia) [1][34].

Figure 2.5 shows a schematic view of a typical solid oxide fuel cell. Electrolyte permits oxide ions movement while blocking electrons movement. Thus, electrolyte materials have to be high ionic conductivity and zero electrical conductivity. Cathode

material reduces oxygen gas to oxygen ions. Oxygen ions are ionically transported from cathode to anode through the oxygen vacancies in the electrolyte. . Due to the dense structure of the electrolyte, reagents can not pass through the electrolyte so fuel and oxidants can not contact directly. Oxygen ions oxidize hydrogen ions at anode side thus water vapor and electrons are produced. Released electrons generate electrical energy owing to pass through the external circuit. The pore structure of the electrode ensures that passage of reagents and gas.

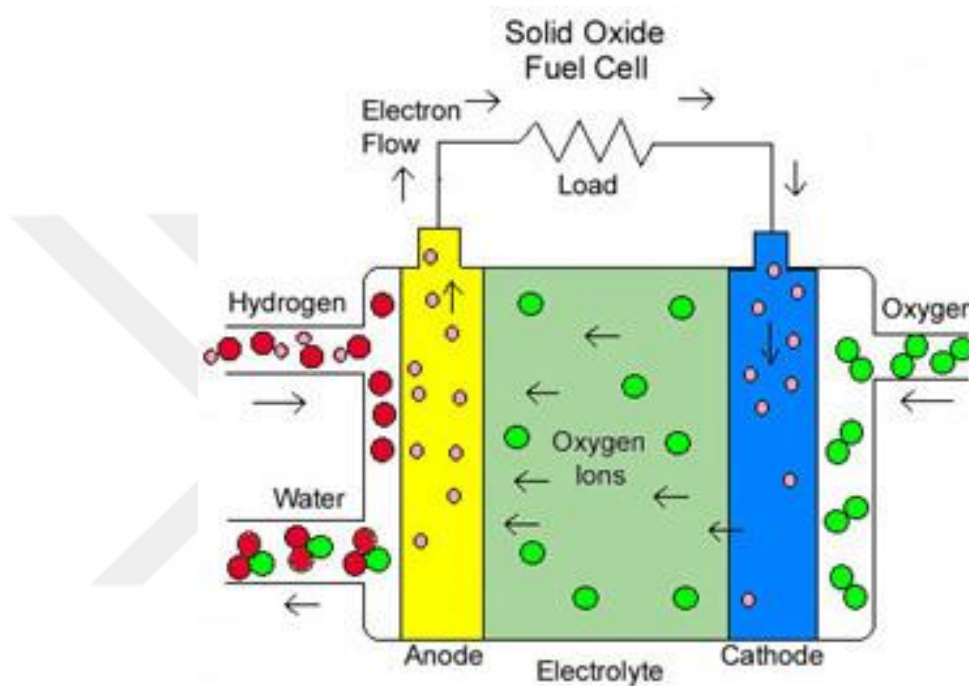
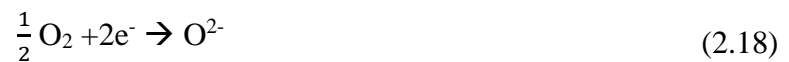


**Figure 2.8 :** A schematic view of solid oxide fuel cell [17].

Anode, cathode and overall reactions are given in equations 2.17-2.19 [35]. In this type of fuel cells, fuel is fed by the anode side and an electrochemical reaction takes place in the thin layer between the anode and the electrolyte.



Various types of fuels are used in SOFC such as hydrogen, CO and CH<sub>4</sub>. Hydrogen is used as fuel due to the fact that it is clean and environmental friendly energy source; furthermore, it provides higher efficiency than other fuels. Carbon monoxide (CO) and methane (CH<sub>4</sub>) can be used as a fuel and they react with water, thus

hydrogen can be produced for feeding anode side as fuel. These reactions was shown in equation 2.20 and 2.21 [36].



The electrolyte should be dense, impermeable, thin for minimizing ohmic loss, high mechanical strength, chemical and thermal compatibility with other cell components. Moreover, it should have high ionic conductivity (greater than  $10^{-2} \text{ Scm}^{-1}$ ) and zero electron conductivity. On the other hand, electrodes should have high electronic conductivity, chemical, mechanical and thermal stability, compatibility and minimum reactivity with other components, and porous structure for permitting gas flow [37].

Yttrium Stabilized Zirconia (YSZ) is common material for electrolyte and it has high ionic conductivity above  $700^\circ\text{C}$  and negligible electronic conductivity. According to Figure 2.6, Scandium-doped Zirconia (SDZ) has better electronic conductivity at low temperatures. Gadolinium-doped Ceria (GDC) has even better conductivity, but the main problem of this material is the reduction of  $\text{Ce}^{4+}$  ions to  $\text{Ce}^{3+}$  ions with hydrogen above  $600^\circ\text{C}$  on the anode side. This causes the formation of electron holes thus ceria become electronically conductive and led to internal short circuit. Furthermore, Lanthanum Gallate with Strontium and Magnesium doped (LGSM) has higher conductivity than other materials at low temperatures [38], [39].

Anode material should have high ionic and electronic conductivity in a reducing environment and porosity for the transport of fuel and oxidant products. Nickel-cermet composites and gadolinium-doped ceria are generally used as an anode material [40]. Nickel and YSZ composites have high electrical conductivity, ionic conductivity and activity. Nickel is preferred as anode material due to the fact that it has excellent catalytic properties for breaking hydrogen bonds. The main problem of nickel anode is the carbon deposition which causes plugging gas pathways, delamination of nickel layer and deformation. For eliminating this problem, nickel is used with GDC and YSZ [40]. Additionally, various perovskite ceramics such as lanthanum-doped strontium titanate, yttrium-doped  $\text{SrTiO}_3$ , strontium and vanadium doped lanthanum chromate (LSCV) are used as anode material.

Cathode is known as air electrode that has porous structure for providing gas passage in oxidizing atmosphere. Oxygen is reduced to oxygen ions with consuming two electrons owing to catalytically active cathode. Cathode should be highly ionic conductive for providing pathway between external circuit and electrochemical reaction field. Cathode's chemical and dimensional stability, thermal expansion coefficient, and reactivity have to be compatible with other cell components. It has porous structure for ensuring gas flow. Oxide based materials are used as electrode material owing to their high resistivity for oxidizing environment. Lanthanum based perovskite oxides such as Lanthanum Strontium Manganite (LSM), Lanthanum Strontium Ferrite/Cobaltite (LSFC), and Lanthanum Strontium Chromite/Manganite (LSCM) are generally used as cathode material [34], [38], [41]. Lower valance cations partially substitute in perovskite ( $ABO_3$ ) structure thus it forms oxygen vacancies that provide oxygen conductivity. If perovskite ceramics have multivalent cations, electronic conductivity increases. To increase electronic and ionic conductivity of perovskite ceramics, various elements doped perovskite structure thus one phase provides ionic conductivity and other phase provides electronic conductivity; moreover, this material is named as Mixed Ionic and Electronic Conductor (MIEC). LSFC or LSM that are mixed with Cerium-Gadolinium Oxide (CGO) are examples of MIEC. Figure 2.6 shows the results of impedance spectroscopy analysis of CGO added LSFC and LSM at 900°C. The CGO contribution does not affect the LSFC, but it increases the polarization resistance and decrease the mass transport resistance in LSM. According to these results, cerium-gadolinium oxide addition of some perovskite enhances material properties and conductivity.

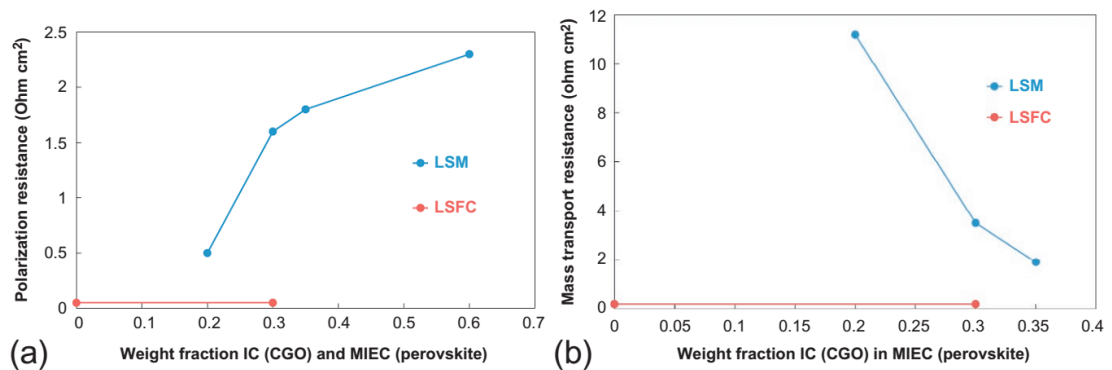


**Figure 2.9 :** Polarization resistance of CGO added LSFC and LSM [42].

Interconnects conduct electricity from one individual cell's anode to neighbor cell's cathode while blocking fuel and oxidant contact. Interconnects can be classified two different groups; ceramic materials which operates at high temperatures (900-1000°C) and metal alloys which operate at low temperatures. Generally, lanthanum and yttrium chromate doped ceramic interconnects are used. Electronic conductivity of interconnect material can be increased with addition of various elements such as Mg, Sr, Ca and Ca/Co. These materials' electronic conductivity increase with increasing temperature [43].

SOFC's performance is affected by various factors such as pressure, temperature, gas composition and utilization, and impurities. Higher cell performance can be observed at higher pressure and this behavior was showed in Figure 2.7. In this investigation Air Electrode Supported (AES) cell, voltages are tested between 1 to 15 atm pressures. It has become apparent that cell voltage increases with increasing pressure.

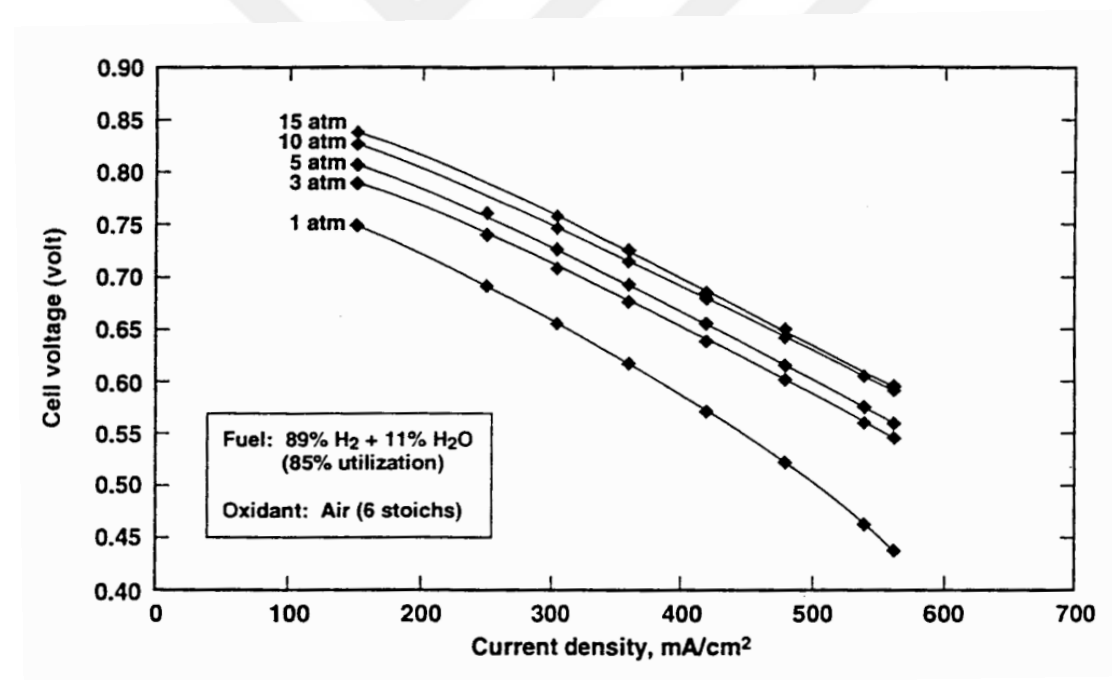


**Figure 2.10 :** AES cell voltage and current density values for various pressures [1].

Another important factor is temperature, when it increases cell performance enhances. Figure 2.8 shows the change in cell voltage depending on the current density at different temperatures of a SOFC which is fed 67% H<sub>2</sub>-22% CO-11% H<sub>2</sub>O as fuel. At 800°C, noticeable decrease in cell voltage is observed, the main reason of that is lower ohmic polarization in lower temperature.

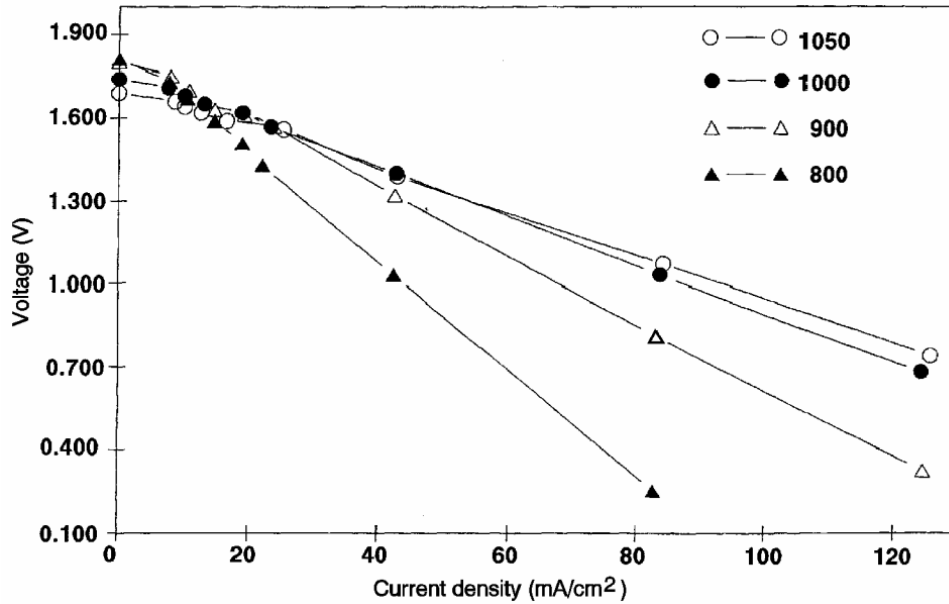


**Figure 2.11 :** Voltage and current density at various temperature [1].

Researches on SOFC are focused on lowering the operating temperature so that material and operation cost, chemical and mechanical stability of cell components can be developed. Decreasing the electrolyte thickness is one of the successful applications that reduce the operating temperature. When the electrolyte thickness decreased, the ohmic loss decreases, thus efficiency of SOFC increases. Figure 2.9 shows the relationship between temperature, electrical conductivity and electrolyte thickness [1]. Thinner electrolyte has higher conductivity than thicker one at the same temperature.

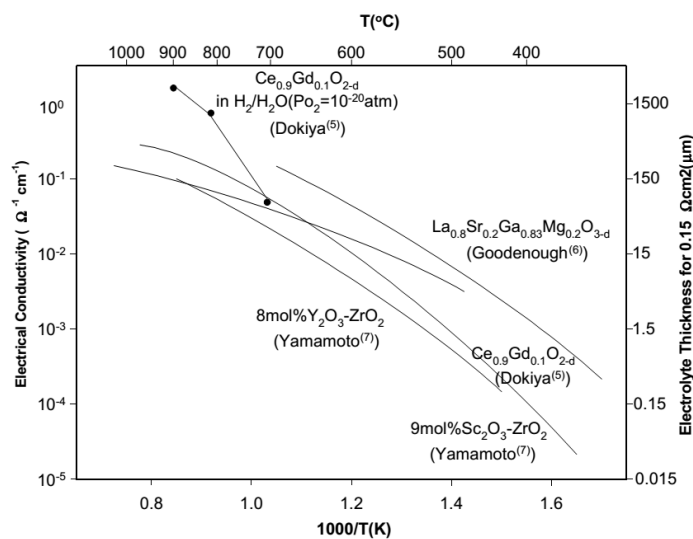


**Figure 2.12 :** Relationship between temperature, electrical conductivity and electrolyte thickness [1].

Another factor is gas composition and utilization. Pure oxygen usage is more efficient than using air in SOFC. Figure 2.14 shows the variation of cell voltage with pure oxygen and air use depending on the current density (45). In this figure (o) represents pure oxygen usage and ( $\Delta$ ) represents air usage as fuels at 1000°C operating temperature.

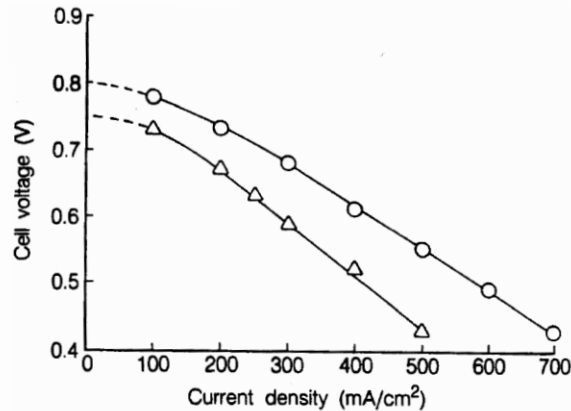


**Figure 2.13 :** Current density and cell voltage change with using pure oxygen (o) and air ( $\Delta$ ) as fuel [1].

Hydrogen and carbon rate in fuel is another factor that affects the cell performance. When hydrogen amount in fuel increases cell potential enhances. Figure 2.11 shows the change of cell potential according to H/C ratio and oxygen/carbon ratio. According to the figure, if O/C ratio equals to one like CO higher cell potential is observed than other compositions.

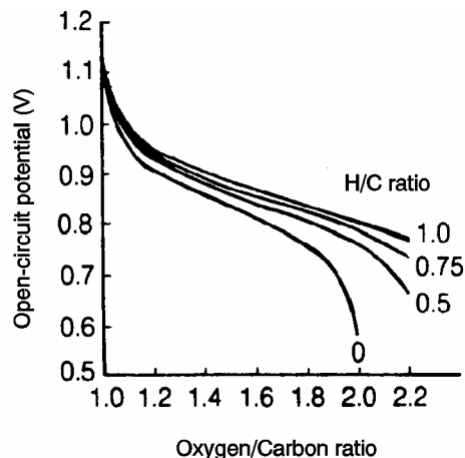


**Figure 2.14 :** Potential and oxygen/carbon ratio values for various H/C ratio [1].

Impurities such as hydrogen sulfide ( $H_2S$ ), hydrogen chloride ( $HCl$ ), and ammonia ( $NH_3$ ) presence in SOFC decrease cell performance. Increment on current density

causes rising in ohmic losses, activation losses, and concentration losses which causes decrease in cell voltage.

The main advantages of SOFC are reliable, modular, and low emission systems that allow high efficiency (up to 70%) energy production when used with integrated combustion units in small power generation systems. Since these fuel cells do not contain liquid phase, the corrosion problem has been eliminated thus it has long-life. They are modular and flexible systems [33].

The main disadvantages of SOFC are that it is difficult to choose suitable material because high-conductive, porous and low expansion coefficient materials should be selected; moreover, these types of materials are expensive.

SOFC systems are used in vehicles such as cars, trucks, airplanes, and ships as batteries and alternators. They are used in stationary power stations which use Distributed Energy Sources (DERs), backup, remote power, grid-independent power, and high-quality power generation systems [44].



### 3. LITERATURE REVIEW

High temperature proton conductive materials have several benefits, which are reducing cell voltage and no large change in oxygen concentration, when they used in SOFC.  $\text{BaCeO}_3$  has high protonic conductivity at low temperatures due to the cubic structure and when it doped with Gd, mixed ionic conductor is obtained and it has protonic conductivity beside oxide ion conductivity. The reason of using gadolinium as dopant is that radius of Gd matches with ceria. On the other hand, at lower oxygen partial pressure ceria reduced from  $\text{Ce}^{4+}$  to  $\text{Ce}^{3+}$  ions and leads to undesired electronic conduction. To overcome this problem mixed ionic conductors such as Gd doped  $\text{BaCeO}_3$  are used thus one phase increases ionic conductivity, and other phase obstructs cerium reduction [4], [45]–[49].

Bonanos [50] studied transport properties and conduction mechanism of  $\text{BaCe}_{0.9}\text{Gd}_{0.1}\text{O}_{2.95}$ . The author reported that this type of material has not only oxide ion conductivity but also protonic conductivity at the temperature range of 600–1000°C; moreover, while oxide ion conductivity was increasing with temperature, protonic conductivity peaked between 800–900°C. Figure 3.1 shows oxide ion and protonic conductivity of  $\text{BaCe}_{0.9}\text{Gd}_{0.1}\text{O}_{2.95}$ .

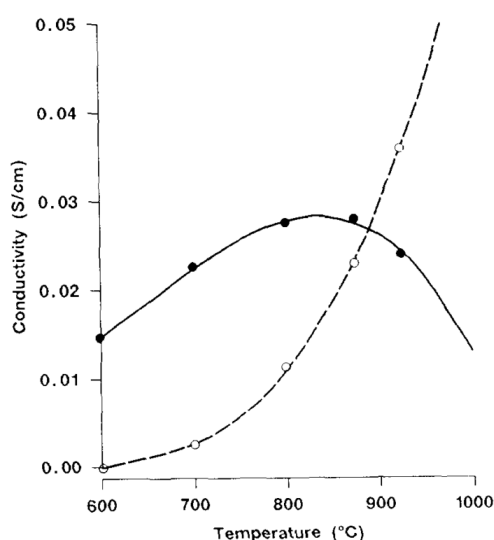


**Figure 3.1 :** Figure 3.1 Ionic conductivity of  $\text{BaCe}_{0.9}\text{Gd}_{0.1}\text{O}_{2.95}$  established into protonic (●) and oxide ion (○) components [50].

Therefore, ion transport mechanism depends not only temperature but also hydrogen and oxygen gas concentration in ambient.

Knight et al. [51] studied lattice constant, space group, and crystal structures of  $\text{BaCe}_{0.9}\text{Gd}_{0.1}\text{O}_{2.95}$  by using high-resolution neutron powder diffraction. The space group was determined as Pmcn and lattice parameters of  $\text{BaCe}_{0.9}\text{Gd}_{0.1}\text{O}_{2.95}$  were found as  $a=8.7732 \text{ \AA}$ ,  $b= 6.2447 \text{ \AA}$ , and  $c=6.2216 \text{ \AA}$ .  $\text{BaCe}_{0.9}\text{Gd}_{0.1}\text{O}_{2.95}$  proton conductivity at low temperature and oxide ion conductivity at high temperature have been reported. According to test results, their proposed crystal structure of  $\text{BaCe}_{0.9}\text{Gd}_{0.1}\text{O}_{2.95}$  can be seen in Figure 3.2.

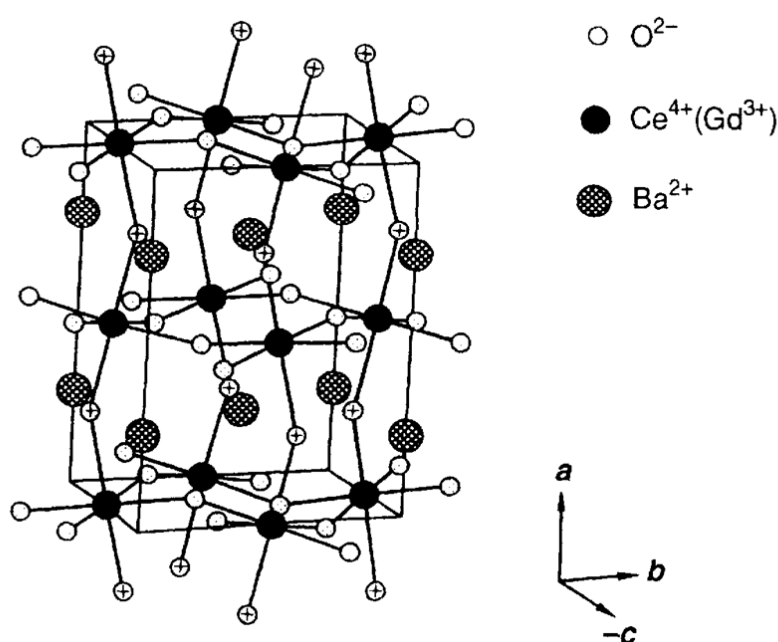


**Figure 3.2 :** Crystal structure of  $\text{BaCe}_{0.9}\text{Gd}_{0.1}\text{O}_{2.95}$  [51].

High temperature transport study of  $\text{BaCe}_{0.9}\text{Gd}_{0.1}\text{O}_{2.95}$  as solid electrolyte for fuel cells was reported by Bonanos [52]. In their work, samples were prepared with conventional solid-state reaction synthesis as single-phase perovskite structure and they were sintered at  $1475^\circ\text{C}$ . Conductivity values of  $\text{BaCe}_{0.9}\text{Gd}_{0.1}\text{O}_{2.95}$  at temperature range of  $600\text{-}1000^\circ\text{C}$  were measured with van der Pauw technique. According to Bonanos this material shows both protonic and oxide ion conduction with the same activation energy, because of that while protons migrate to interstitials owing to small radius, oxide ions migrate through to vacancies in crystal structure due to their large radius. It shows that conductivity and transport mechanism of Gd doped barium cerate varies with oxygen concentration and hydrogen atmospheres.

Kumar et al [53] investigated microwave assisted sintering gadolinium doped barium cerate crystal structure and phase study with using XRD and Energy Dispersive Spectrum (EDS). XRD results in Figure 3.3 show that fluorite and orthorhombic perovskite structure matched with Ba10CG (mole fractions are 0.1 BaO, 0.8 CeO<sub>2</sub>, 0.2 GdO<sub>1.5</sub>) and BCG15 (mole fractions are 1.0 BaO, 0.85 CeO<sub>2</sub>, 0.15 GdO<sub>1.5</sub>).

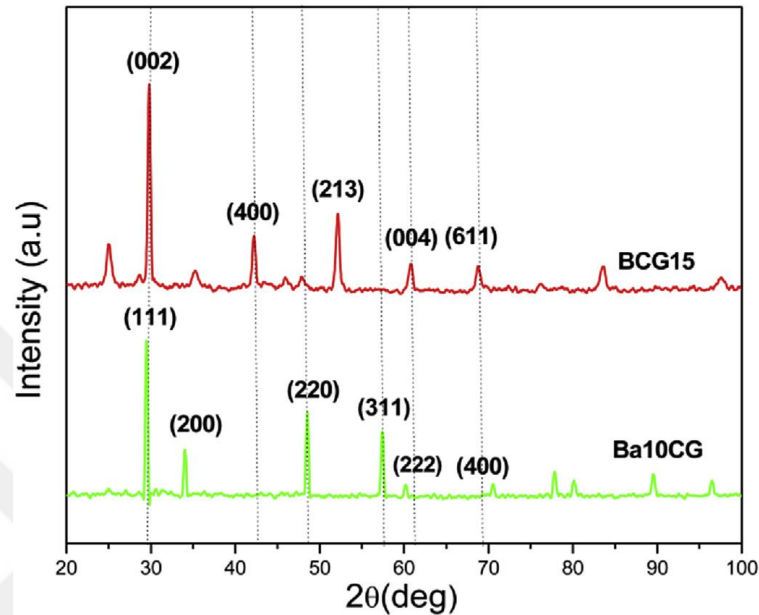


**Figure 3.3 :** XRD patterns for Ba10CG and BCG15 sintered samples at 1400°C [53]. EDS analysis of Ba10CG and BCG15 verified XRD results of these samples and it can be seen in Figure 3.4.

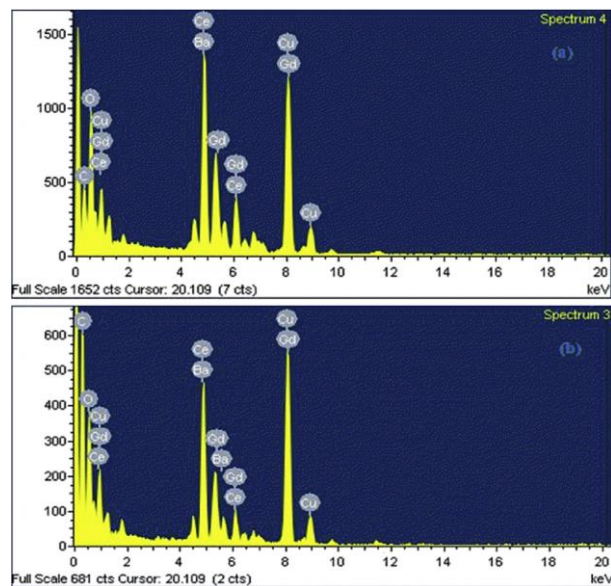


**Figure 3.4 :** EDS analysis of (a) Ba10CG and (b) BCG15 [53].

While gadolinium doped barium cerate phase increased ionic conductivity, gadolinium doped ceria phase decreased electronic conductivity which causes barium cerium gadolinium oxide to be suitable material for fuel cell applications as electrolyte.

Bonanos et al. [54] studied structure, transport properties and fuel cell applications of  $\text{BaCe}_{(1-x)}\text{Gd}_x\text{O}_{(3-x/2)}$ . The Gd solubility limit in  $\text{BaCeO}_3$  was determined as between  $x=0.15$  and  $0.20$ , and more than  $0.2$  mole fraction of Gd material disproportionated into  $\text{BaGd}_2\text{O}_4$  and  $\text{BaO}$ . Moreover, due to the fact that  $\text{BaO}$  is unstable in air, it absorbs water and  $\text{CO}_2$  so barium carbonate and barium hydroxide phases can be observed. These phases have low conductivity so over than  $x=0.15$  conductivity was decreased. According to various studies [55], [56], Gd solubility in  $\text{BaCeO}_3$  was increased with increasing temperature. This material shows both oxide ion and protonic conductivity; moreover, while oxide ion conductivity was affected by water vapor concentration, protonic conductivity was not affected. Therefore, this material shows chemical stability for fuel cells that use hydrogen as fuel.

Taniguchi et al. [56] performed proton conductivity of gadolinium-doped barium cerates at high temperature. Samples were prepared with conventional solid-state reaction technique and they were sintered in air for 10h at  $1650^\circ\text{C}$ .  $\text{BaCe}_{1-x}\text{Gd}_x\text{O}_{3-\alpha}$  ( $x=0.05, 0.1, 0.15, 0.2, 0.25$ ) single phase perovskite structure samples were synthesized and X-ray diffraction patterns of these samples can be observed in Figure 3.5.

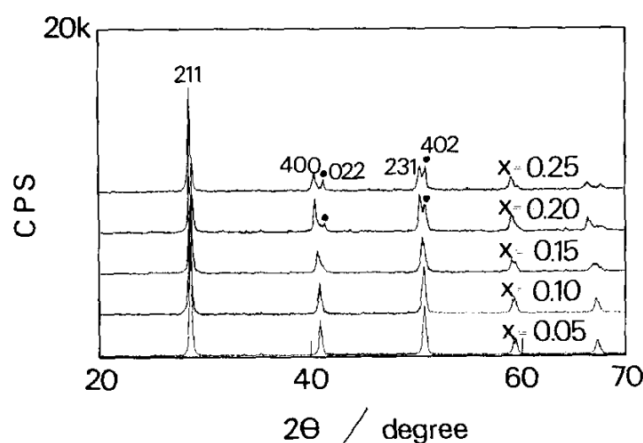


**Figure 3.5 :** XRD patterns of  $\text{BaCe}_{1-x}\text{Gd}_x\text{O}_{3-\alpha}$  [56].

Crystal structure of samples changed from orthorhombic to tetragonal with increasing  $x$ ; moreover, over than  $x=0.2$ , different phases than other samples could

be observed in XRD analysis. Generally, YSZ is common material for fuel cell applications but this study showed conductivity of  $\text{BaCe}_{1-x}\text{Gd}_x\text{O}_{3-\alpha}$  ( $x=0.2,0.25$ ) was higher than YSZ. Arrhenius plots of the conductivity of various  $\text{BaCe}_{1-x}\text{Gd}_x\text{O}_{3-\alpha}$  can be seen in Figure 3.6.

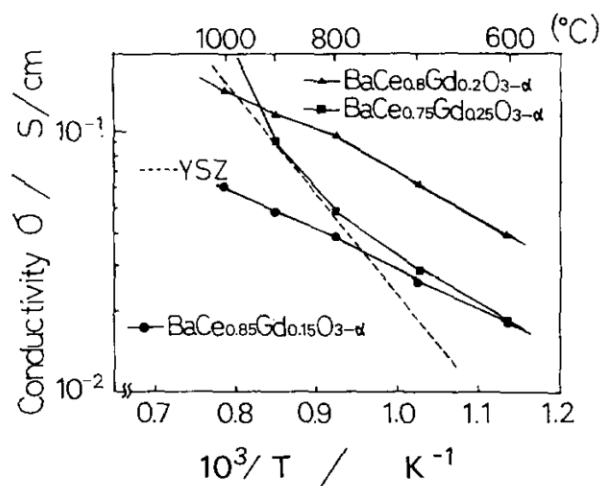


**Figure 3.6 :** Arrhenius plots of the conductivity of  $\text{BaCe}_{1-x}\text{Gd}_x\text{O}_{3-\alpha}$  ( $x=0.15, 0.2, 0.25$ ) [56].

$\text{BaCe}_{1-x}\text{Gd}_x\text{O}_{3-\alpha}$  ceramics had high ionic conductivity and almost zero electronic conductivity thus they are good candidates to solid electrolytes for fuel cells. Figure 3.7 shows transport numbers of oxide ion and proton at the temperature range of 600-1000°C. At 600°C, protons were mobile and no oxide ion conductivity was observed, on the other hand, high oxide ion and low proton conductivity were appeared at 1000°C.  $\text{BaCe}_{1-x}\text{Gd}_x\text{O}_{3-\alpha}$  had mixed ion conductivity at 800°C.

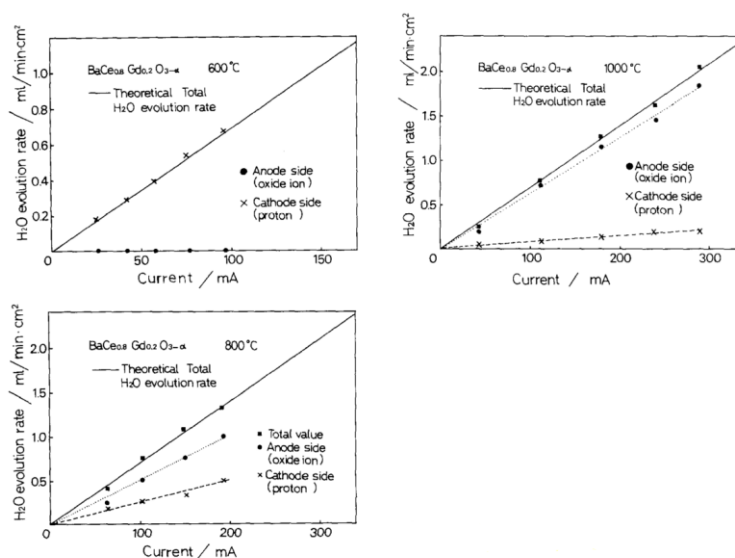


**Figure 3.7 :** Water vapor evaluation rate at 600, 800, and 1000°C [56].

Maffei et al. [57] presented performance characteristic of Gd-doped barium cerate which is prepared with conventional solid-state synthesis technique. They were calcined at 1350°C and sintered at temperature range of 1500-1650°C for 10h. In this study, three different cathodes, which are platinum,  $\text{La}_{0.6}\text{Ca}_{0.4}\text{Fe}_{0.8}\text{Co}_{0.2}\text{O}_3$  (LCFC) and  $\text{La}_{0.6}\text{Sr}_{0.4}\text{CoO}_3$  (LSC) were used; furthermore, highest electronic conductivity and oxygen activity were found in LSC as cathode material. Figure 3.8 indicates XRD patterns of calcined and sintered samples with various temperatures. It had become apparent that while lower than 1600°C samples had minor secondary phases, over than this temperature, single-phase structure was observed.

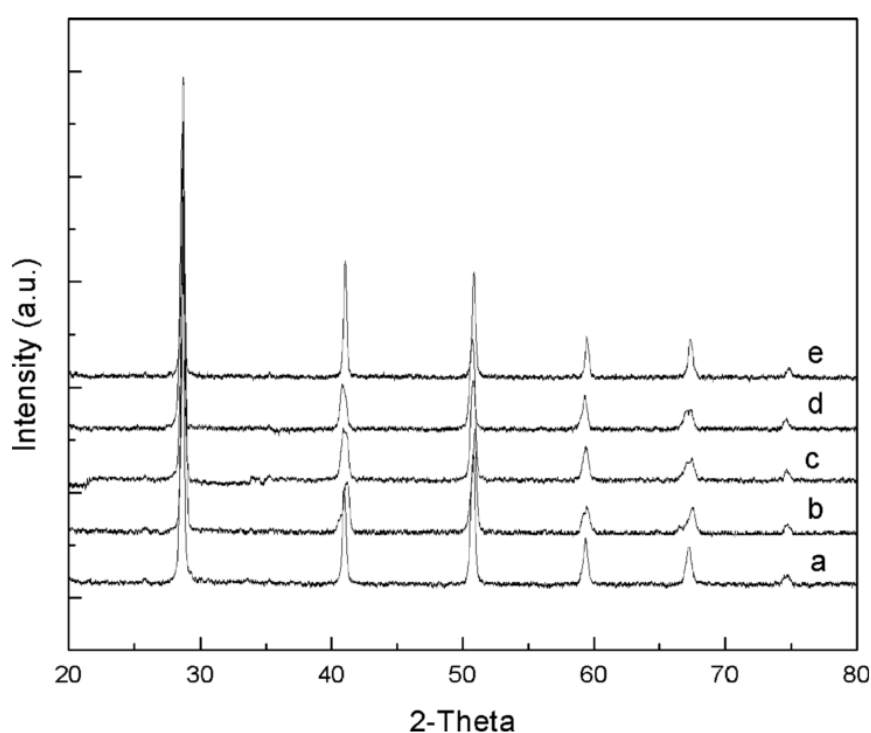


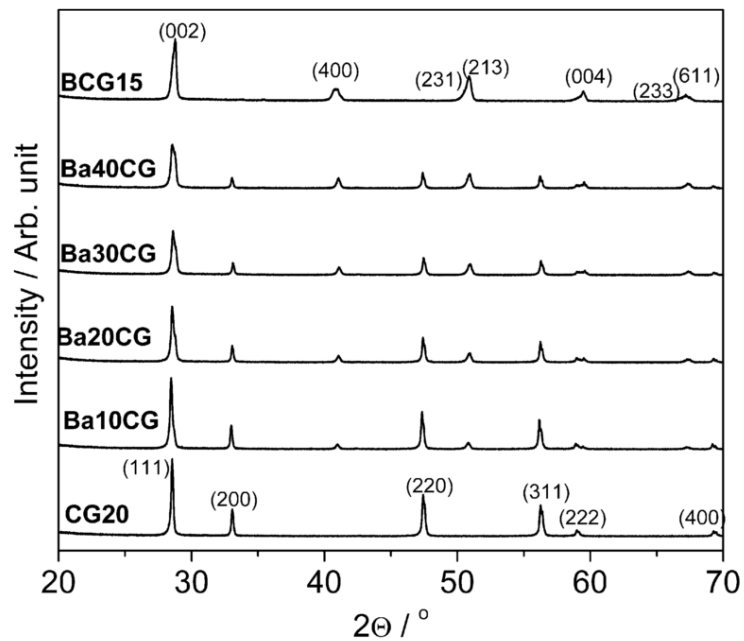
**Figure 3.8 :** XRD patterns of (a) 1350°C, (b) 1500°C, (c) 1550°C, (d) 1600°C and (e) 1650°C [57].

Venkatasubramanian et al. [58] also investigated synthesis and characterization of  $\text{BaO-CeO}_2\text{-GdO}_{1.5}$  system. Samples, which were prepared with conventional solid-state reaction route, were calcined twice at 1350°C for 6h and sintered at 1550°C for 10h in air. Table 3.1 shows mole fraction and name of the samples.

**Table 3.1** : Compositions of samples.

Sample	BaO	CeO <sub>2</sub>	GdO <sub>1.5</sub>
Ba10CG	0.1	0.8	0.2
Ba20CG	0.2	0.8	0.2
Ba30CG	0.3	0.8	0.2
Ba40CG	0.4	0.8	0.2
CG20	0	0.8	0.2
BCG15	1	0.85	0.15

According to XRD patterns, CG20 matched with fluorite structure and with increasing Gd dopant, minor peaks and secondary phase occurred. Besides, BCG15 matched with orthorhombic perovskite structure which supports other authors' results. Figure 3.9 shows XRD patterns of prepared samples.

**Figure 3.9** : XRD of sintered samples [58].

According to Back Scattered Electron images and EDS analysis bright regions included Ce, Gd, and O, besides dark regions included Ba, Ce, Gd, and O as shown in Figure 3.10. Dark regions expanded with increasing amount of Gd.

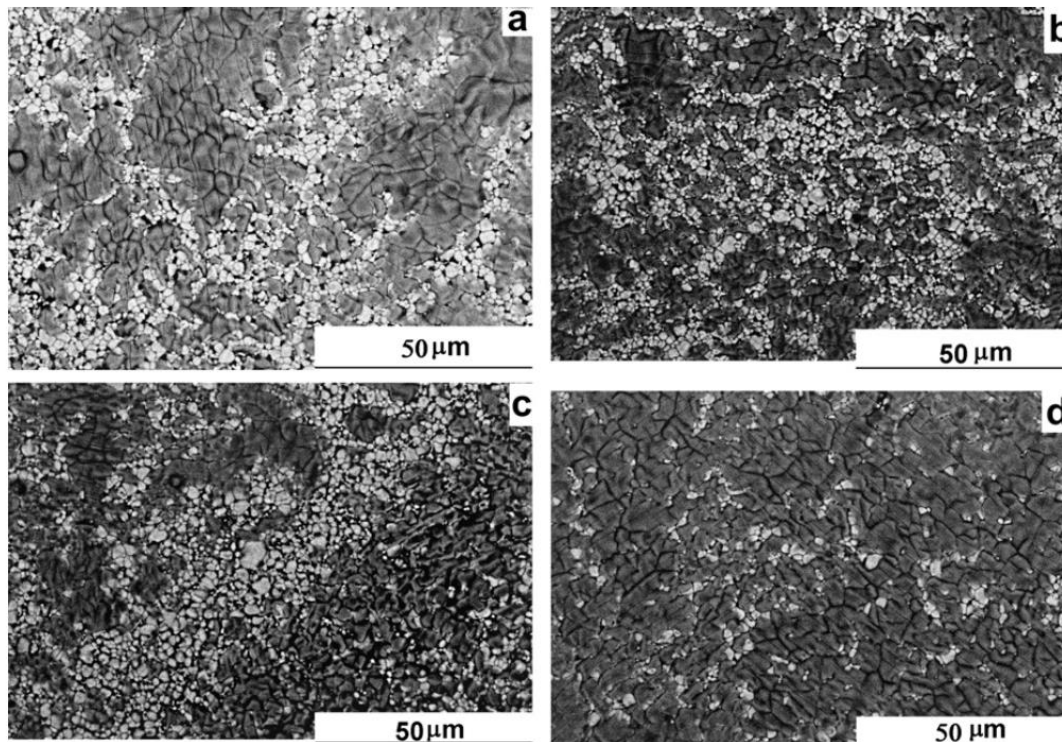


**Figure 3.10 :** Back Scattered Electron images of (a) Ba10CG, (b) Ba20CG, (c) Ba30CG and (d) Ba40CG [58].

Construction and operation of Gd doped barium cerate were reported by Bonanos et al. [59]. This study showed that Gd doped barium cerate had higher cell voltage than gadolinium-doped ceria. According to long-term operation of fuel cell, which is used Gd doped barium, cerates as electrolyte, any deterioration or performance losses were not observed.

Taniguchi et al. [60] prepared  $\text{BaCe}_{0.8}\text{Gd}_{0.2}\text{O}_3$  (BCG) ceramics with using solid-state reaction method. According to this study, BCG ceramics had higher conductivity than YSZ. BCG had not only oxide ionic conductivity but also protonic conductivity, on the other hand oxide ionic conductivity decreased at low oxygen partial pressure and temperature. The authors reported that BCG ceramics had ionic conductivity even at  $300^\circ\text{C}$  differently from earlier research of Taniguchi et al. [56].

Shima et al. [61] investigated the influence of cation on the properties of gadolinium doped barium cerate. In this study,  $\text{Ba}_x\text{Ce}_{0.85}\text{Gd}_{0.15}\text{O}_{3-\delta}$  ( $x=0.96, 0.99, 1.00, 1.01$  and  $1.04$ ) are prepared with conventional solid state reaction, they were calcined at  $1300^\circ\text{C}$  for 16h and sintered at  $1650^\circ\text{C}$  for 4 h. Yellow precipitates which are  $\text{CeO}_2$ , were observed on the sample surface but sintered samples had grey-black color. The authors determined crystal structure of samples as tetragonal cell differs from Knight

and Bonanos [51]. According to XRD results, undoped and  $x=0.96$  doped samples included  $\text{CeO}_2$  and  $\text{BaCe}_{0.9}\text{Gd}_{0.1}\text{O}_{2.95}$  peaks. Figure 3.11 shows XRD pattern of doped and undoped samples. According to Figure 3.11 (a), (004) peak shifted to smaller 2-theta values with increasing Ba content and this indicated that increase of the overall unit cell volume and c lattice constant. But sintered sample pattern differentiated from calcined samples and (004) peak shifted to larger 2-theta values which indicated that decrease of the overall unit cell volume and c lattice constant in Figure 3.11 (b). The authors determined protons were dominant charge carriers even at high temperature differently from Taniguchi et al. [56]. Conductivity increased with increasing amount of Ba content.

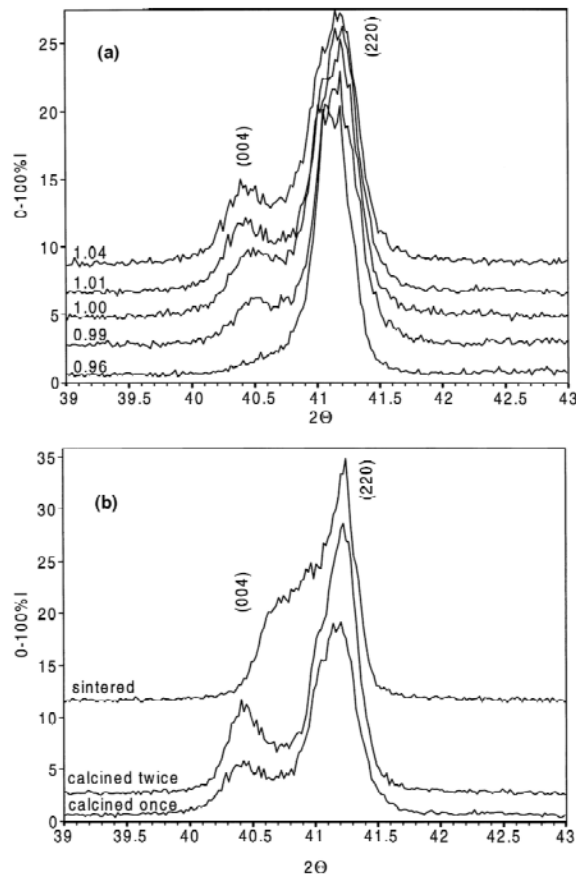


**Figure 3.11 :** XRD patterns of (a)  $\text{Ba}_x\text{Ce}_{0.85}\text{Gd}_{0.15}\text{O}_{3-\delta}$  at  $1350^\circ\text{C}$  and (b)  $\text{Ba}_{1.01}\text{Ce}_{0.85}\text{Gd}_{0.15}\text{O}_{3-\delta}$  after each processing step [61].

Chen et al. [62] also investigated proton conduction in  $\text{BaCe}_{1-x}\text{Gd}_x\text{O}_{3-\alpha}$  ( $x=0.05, 0.10, 0.15$  and  $0.20$ ) ceramics which were prepared with microemulsion method thus high component homogeneity, pure phase and low sintered temperature ceramics were synthesized. Single-phase orthorhombic structure was observed after sintering

process at 1500°C. When the oxygen partial pressure is in the range of  $1-10^{-20}$  atm,  $\text{BaCe}_{1-x}\text{Gd}_x\text{O}_{3-\alpha}$  ceramics showed pure ion conduction property.

Taniguchi et al. [63] performed operating properties of SOFC using  $\text{BaCe}_{0.8}\text{Gd}_{0.2}\text{O}_{3-\alpha}$  electrolytes which are prepared by solid-state reaction method. BCG showed almost zero electron conductivity in  $\text{CO}_2$  atmosphere and it had both protonic and oxide ion conductivity at 800°C. While BCG crystal structure almost had not changed at cathode side in SOFC, it desorbed oxygen at high temperature and low oxygen partial pressure at anode side in SOFC thus crystal structure transformed from orthorhombic to cubic structure and this showed slight mechanical stress but material had chemical stability. BCG decomposed to ceria and  $\text{BaCO}_3$  as a result of reaction with  $\text{CO}_2$ .

Bonanos et al. [55] performed XRD, impedance spectroscopy, concentration cell, and faradaic oxygen transport cell methods to determine ionic conductivity of Gd doped  $\text{BaCeO}_3$  (BCO) ceramics. Gadolinium doped barium cerate had cubic crystal structure; moreover, XRD peak widths were increased with increasing dopant amount and  $\text{BaGd}_2\text{O}_4$  phase was seen with  $x$  value between 0.2-0.4.  $\text{BaCeO}_3$ : Gd had partial electronic conductivity property and highest ionic conductivity was detected for  $x=0.15$  at 600°C. At low oxygen pressure, samples were pure ionic conductor and they had reduction stability thus they were good candidates for SOFC applications.

Fu et al. [64] also studied chemical stability, mechanical and conductivity properties of rare-earth ions doped  $\text{BaCeO}_3$  which was sintered at 1400°C for 6h. According to XRD results, all samples had single phase orthorhombic perovskite structure with a space group of Pnma. Furthermore,  $\text{BaCeO}_3$  and  $\text{BaCe}_{0.9}\text{Gd}_{0.1}\text{O}_{2.95}$  disintegrated to  $\text{CeO}_2$  and  $\text{BaCO}_3$ . If the amount of Gd was increased than it caused evolution of protonic defects and the main reason of that oxygen vacancies adsorbed of water. According to SEM images and EDS analysis of Gd doped BCO, gadolinium doped barium cerate decomposed to  $\text{CeO}_2$  which had bright round shapes in SEM image as shown in Figure 3.12.

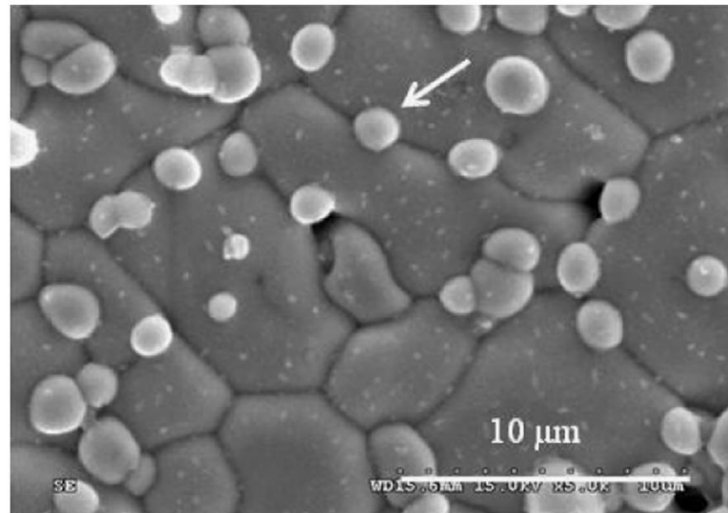


**Figure 3.12** : SEM image of BCO(Gd) [64].

As a result, gadolinium doped barium cerate ceramics have high ionic conductivity, negligible electronic conductivity, good fabrication properties, adequate mechanical strength, and mixed ionic conductivity thus they appeared to be a good candidate for SOFC applications. In spite of that BaO-CeO<sub>2</sub>-GdO<sub>1.5</sub> ternary phase system was not studied detailed in literature.



## 4. EXPERIMENTAL STUDIES

In this chapter, powder preparation and characterization techniques were discussed. Powders were prepared with conventional solid state technique with using oxide powders. After that XRD, SEM and EDS methods were used for characterization of samples.

### 4.1 Powder Preparation

BaCO<sub>3</sub> (99.8%), CeO<sub>2</sub> (99.9%), and Gd<sub>2</sub>O<sub>3</sub> (99.9%) were used as starting powders. Figure 4.1 shows applied steps of conventional solid state method.

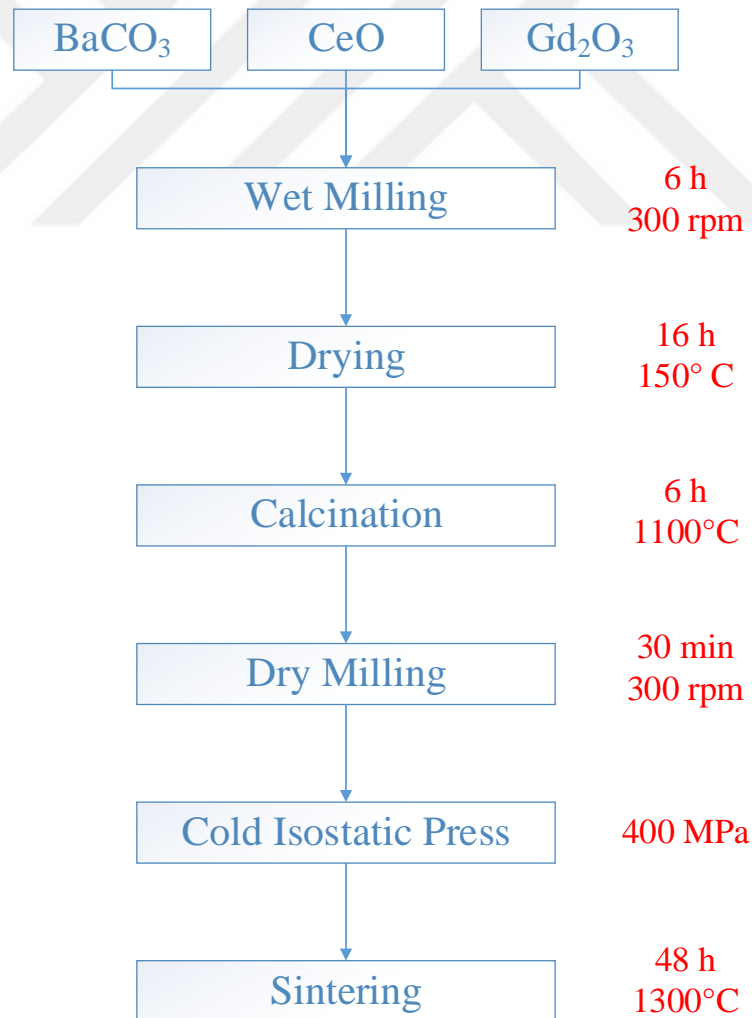


**Figure 4.1 :** Conventional solid state technique steps.

Powders were mixed with alcohol and they were milled for 6 hours at 300 rpm to reduce the particle size. Figure 4.2 shows used ball mill for reducing particle size.



**Figure 4.2 :** Used ball mill in experiment.

Then the alcohol was removed by the samples with drying 16 hours at 150°C. Figure 4.3 shows powders after drying.



**Figure 4.3 :** Powders view after drying.

Prepared powders were calcined at 1100°C for 6 hours. Figure 4.4 shows calcined powders.



**Figure 4.4 :** Calcined powders.

Samples were milled for 30 minutes after calcination and pelletized by cold isostatic press under 400 MPa. Figure 4.5 shows used cold isostatic press.



**Figure 4.5 :** Cold isostatic press.

Alumina crucibles were used for sintering and samples were sintered at 1300°C for 48 hours. Figure 4.6 shows pellets after sintering process.

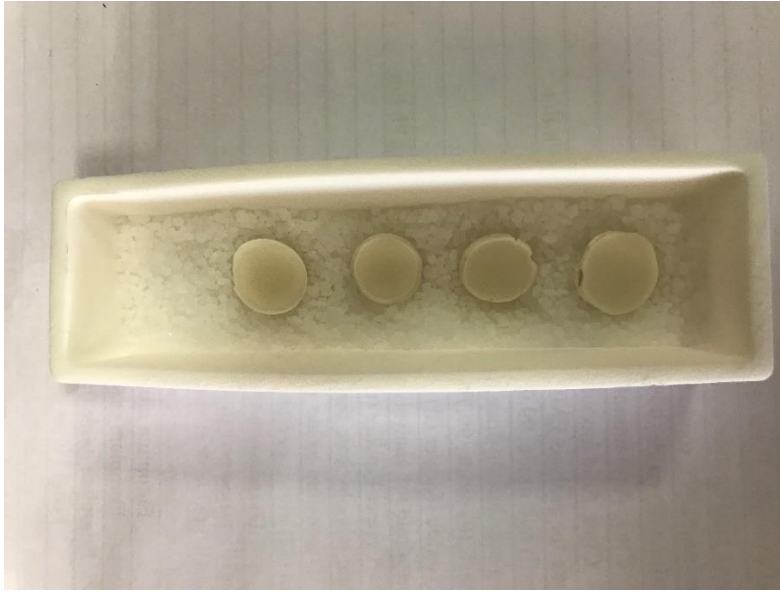


**Figure 4.6 :** Sintered pellets.

According to our observations, some samples' surface color changed from white to yellow and this layer was estimated as  $\text{CeO}_2$  precipitates. On the other hand, especially  $\text{BaCe}_{0.8}\text{Gd}_{0.2}\text{O}_{2.90}$ ,  $\text{BaCe}_{0.7}\text{Gd}_{0.3}\text{O}_{2.85}$ , and  $\text{BaCe}_{0.5}\text{Gd}_{0.5}\text{O}_{2.75}$  samples' color changed from white to grey-black after sintered. These color changes can be noticed in Figure 4.7.

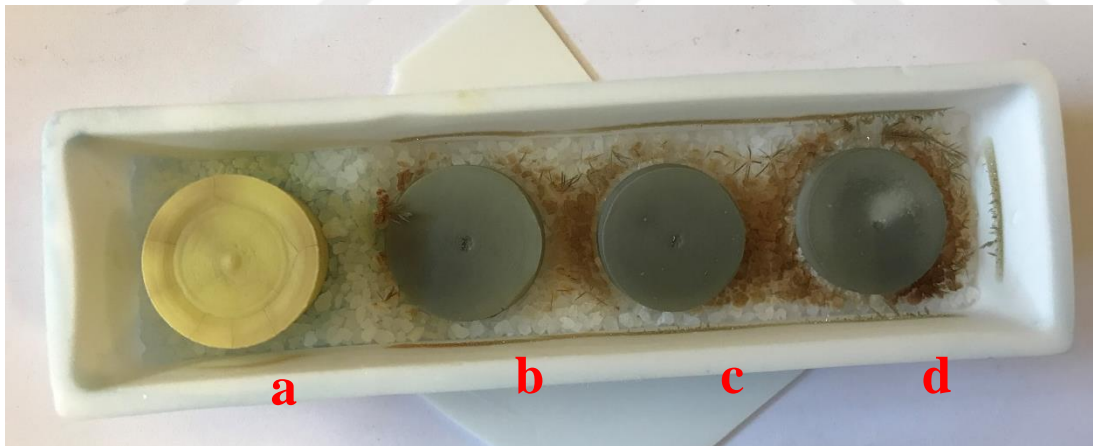


**Figure 4.7 :** Sintered pellets (a)  $\text{BaCe}_{0.9}\text{Gd}_{0.1}\text{O}_{2.95}$ , (b)  $\text{BaCe}_{0.8}\text{Gd}_{0.2}\text{O}_{2.90}$ , (c)  $\text{BaCe}_{0.7}\text{Gd}_{0.3}\text{O}_{2.85}$ , and (d)  $\text{BaCe}_{0.5}\text{Gd}_{0.5}\text{O}_{2.75}$ .

This process was applied to every composition to construct ternary phase diagram of  $\text{BaO-CeO}_2\text{-Gd}_2\text{O}_3$ .

$\text{BaCe}_{(1-x)}\text{Gd}_{(x)}\text{O}_{(3-x/2)}$ (BCG) samples were named according to their composition. For instance, BCG40-10 includes 50%  $\text{BaO}$ , 40%  $\text{CeO}_2$  and 10%  $\text{GdO}_{1.5}$ . Table 4.1 shows samples' names and compositions.

**Table 4.1** : Compositions of samples.

Sample	BaO (%)	CeO <sub>2</sub> (%)	GdO <sub>1.5</sub> (%)
BCG45-5	50	45	5
BCG40-10	50	40	10
BCG35-15	50	35	15
BCG25-25	50	25	25
BCG70-10	20	70	10
BCG50-30	20	50	30
BCG30-50	20	30	50
BCG10-70	20	10	70
BCG10-20	70	10	20
BCG10-40	50	10	40
BCG10-50	40	10	50
BCG10-60	30	10	60
BCG5-62	33	5	62
BCG10-57	33	10	57
BCG0-67	33	0	67
BCG0-50	50	0	50

BCG0-67, BCG0-50 and BCG10-57 samples were quenched for determination of stability of BaGd<sub>2</sub>O<sub>4</sub> phase stability.

BCG25-25 and BCG0-67 samples were also prepared with Pechini (Sol-Gel) method as control samples. Figure 4.8 shows steps of sol-gel method.

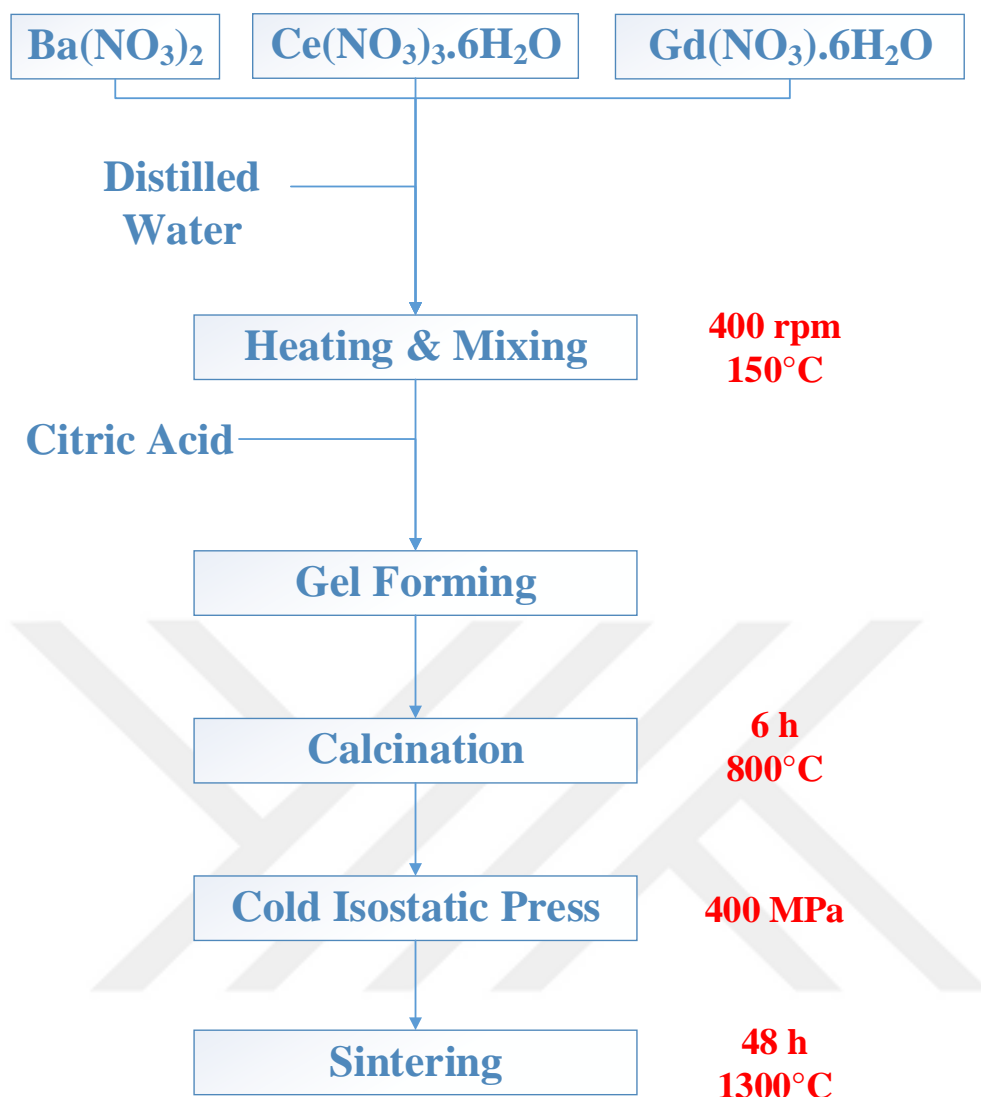
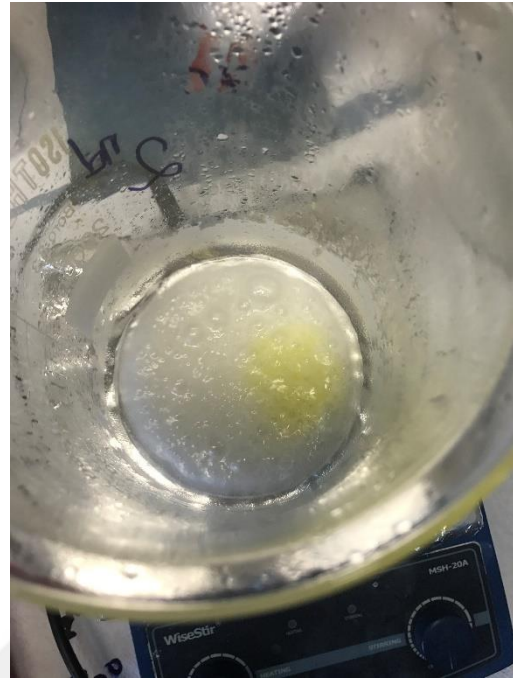


**Figure 4.8 :** Sol-gel technique steps.

In this method,  $\text{Ba}(\text{NO}_3)_2$ ,  $\text{Ce}(\text{NO}_3)_3 \cdot 6\text{H}_2\text{O}$  and  $\text{Gd}(\text{NO}_3)_3 \cdot 6\text{H}_2\text{O}$  powders were used as starting powders. These powders were mixed with distilled water. Then, they were stirred and heated with using magnetic stirrer. During mixing and heating periodically citric acid was added to solution as chelating agent. Citric acid amount was calculated as one mole per cation. Metal ions and citric acid formed organic complex bonds between each other thus solution viscosity increased. Figure 4.9 shows before and after adding chelating agent solutions.



(a)



(b)

**Figure 4.9 :** (a) before and (b) after adding chelating agent.

Distilled water in solution was removed with stirring and heating. When water amount in solution decreased critic level, sudden combustion reaction occurred. Figure 4.10 shows sample's view after sudden combustion reaction.



**Figure 4.10 :** Sample's view after sudden combustion reaction.

After then, samples put into drying oven at 150°C thus organics and water were removed from solution and reaction completed. As a result of reaction, samples formed foam shape. Figure 4.11 shows sample's view after combustion reaction.



**Figure 4.11** : Sample's view after combustion reaction.

Then powders were ground and put into alumina crucible for calcination reaction. Samples were calcined at 800°C for 6 hours. Figure 4.12 shows before and after calcination sample.



**Figure 4.12** : (a) before and (b) after calcination step sample's view.

Calcined powders pressed at 400 MPa with cold isostatic press thus pellets were produced. Then, pellets were sintered at 1300°C for 48 h. Samples were divided two groups, first group was quenched and the second group was cooled in furnace. Results of control samples were compared with the samples that were prepared with solid-state reaction method.

#### **4.2 Phase Analysis and Characterization**

X-ray diffraction, Scanning Electron Microscopy (SEM) and Energy Dispersive Spectroscopy (EDS) methods were used for characterization and phase analysis of samples. Bruker D8 Advance X-ray Diffractometer was used for XRD analysis. Cu- $K_{\alpha}$  (1.5418 Å) radiation was used and measurements were completed between  $2\theta=20^{\circ}$ - $80^{\circ}$  degree. Crystal phases, peak positions and intensities of samples were compared with Joint Committee on Powder Diffraction Standards (JCPDS) database.

SEM/EDS analyses of samples were completed with using Zeiss Ultra Plus Field Emission Scanning Electron Microscope.



## 5. RESULTS AND DISCUSSIONS

In this section, XRD and SEM/EDS results were discussed. According to analysis results, BaO-CeO<sub>2</sub>-GdO<sub>1.5</sub> quasiternary phase diagram was constructed.

First of all quasi-binary phase diagrams for every phases were investigated for determination of intermediate phases and also phase transitions at 1300°C. For this purpose, CeO<sub>2</sub>-GdO<sub>1.5</sub> and BaO-CeO<sub>2</sub> quasi-binary phase diagrams were examined, but BaO-GdO<sub>1.5</sub> quasi-binary phase diagram does not exist in literature. Thus BaO-GdO<sub>1.5</sub> quasi-binary phase diagram was studied.

CeO<sub>2</sub>-GdO<sub>1.5</sub> quasi-binary phase diagram was examined for understanding phases at 1300°C. Figure 5.1 shows CeO<sub>2</sub>-GdO<sub>1.5</sub> quasi-binary phase diagram [3]. According to this diagram, single fluorite type (*f*-type) CeO<sub>2</sub> phase was detected up to 26 mol% ceria content, between 26-50 mol % not only *f*-type CeO<sub>2</sub> but also cubic type (*c*-type) Gd<sub>2</sub>O<sub>3</sub> could be observed at 1300°C. On the other hand, between 50-92 mol% only single *c*-type phase Gd<sub>2</sub>O<sub>3</sub> had been existed; moreover, over than 92 mol% Gd<sub>2</sub>O<sub>3</sub> to pure gadolinium oxide monoclinic phase (*b*-type) was reported.

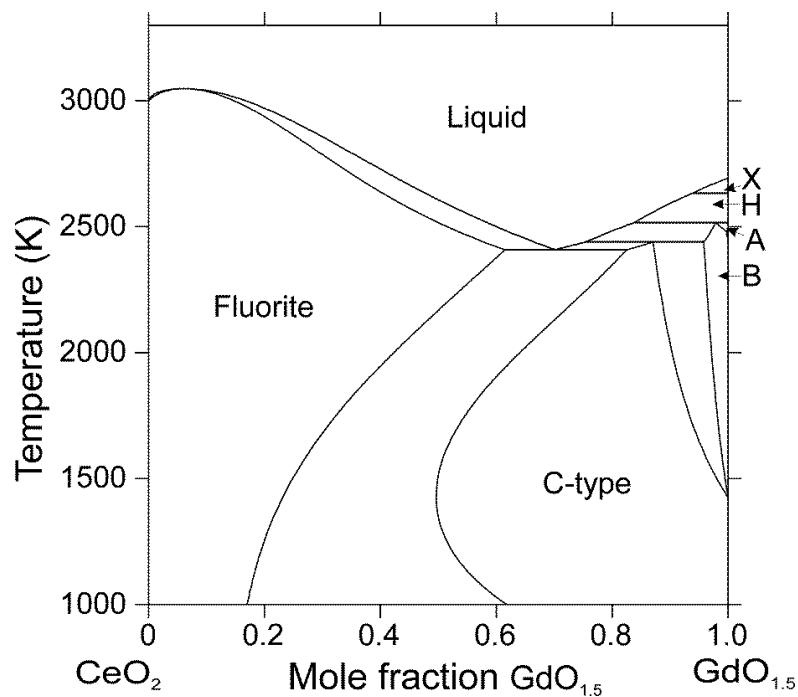


**Figure 5.1 :** CeO<sub>2</sub>-GdO<sub>1.5</sub> quasi-binary phase diagram [3].

According to BaO-CeO<sub>2</sub> [65] quasi-binary phase diagram, BaCeO<sub>3</sub> solid solution exists at 1300°C. Figure 5.2 shows BaO-CeO<sub>2</sub> quasi-binary phase diagram. BaCeO<sub>3</sub> phase was detected at 50 mol % CeO<sub>2</sub>.

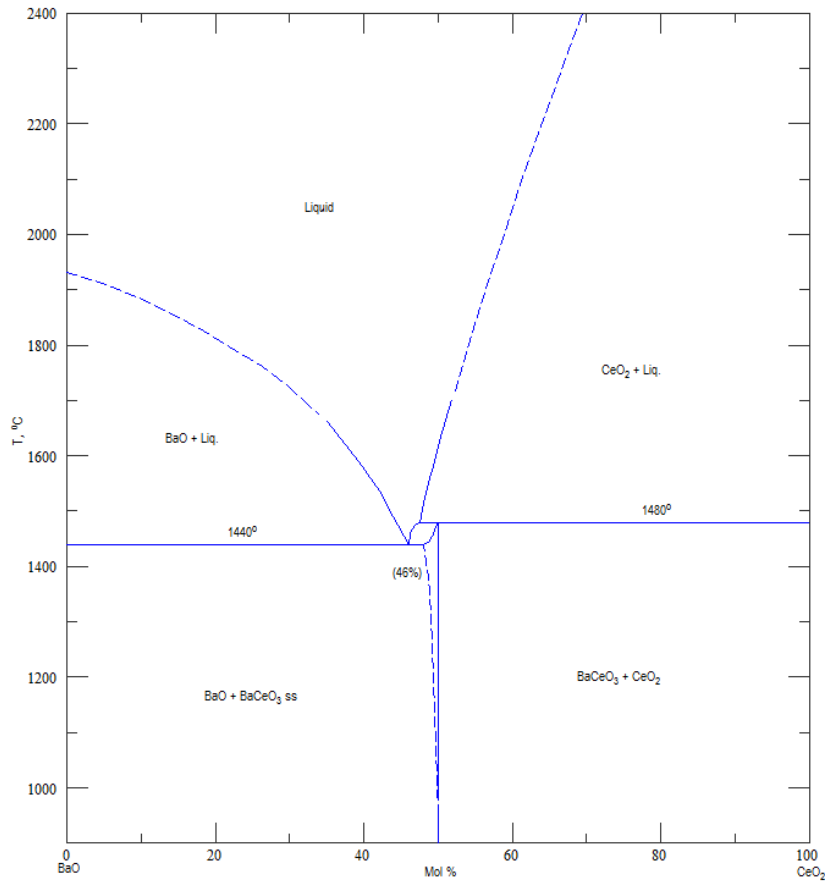


**Figure 5.2 :** BaO-CeO<sub>2</sub> quasi-binary phase diagram [65].

For determination of BaO-GdO<sub>1.5</sub> quasi-binary phase diagram, BCG0-67 and BCG0-50 samples were prepared. Furthermore, these samples were quenched also for determination of BaGd<sub>2</sub>O<sub>4</sub> phase stability. According to XRD and SEM/EDS results, this phase is high temperature stable phase and it decomposes to BaO and monoclinic Gd<sub>2</sub>O<sub>3</sub>. Figure 5.3 and 5.4 indicate quenched and furnace cooled samples. Quenched samples were named as QBCG0-67 and QBCG0-50. It has become apparent that quenched samples included BaGd<sub>2</sub>O<sub>4</sub> and small portion of monoclinic Gd<sub>2</sub>O<sub>3</sub>; on the other hand, BaCO<sub>3</sub> and *b*-type Gd<sub>2</sub>O<sub>3</sub> existed in furnace-cooled samples. The reason of that BaGd<sub>2</sub>O<sub>4</sub> is high temperature stable phase and during cooling it decomposes to BaCO<sub>3</sub> and monoclinic Gd<sub>2</sub>O<sub>3</sub> phases. For understanding BaGd<sub>2</sub>O<sub>4</sub> phase stability quenched samples which are QBCG0-67 and QBCG0-50 were measured with XRD

after 1 week from first measurement. These samples were named as QBCG0-67-2 and QBCG0-50-2. It was realized that  $\text{BaGd}_2\text{O}_4$  phase decomposed to  $\text{BaCO}_3$  and monoclinic  $\text{Gd}_2\text{O}_3$ .

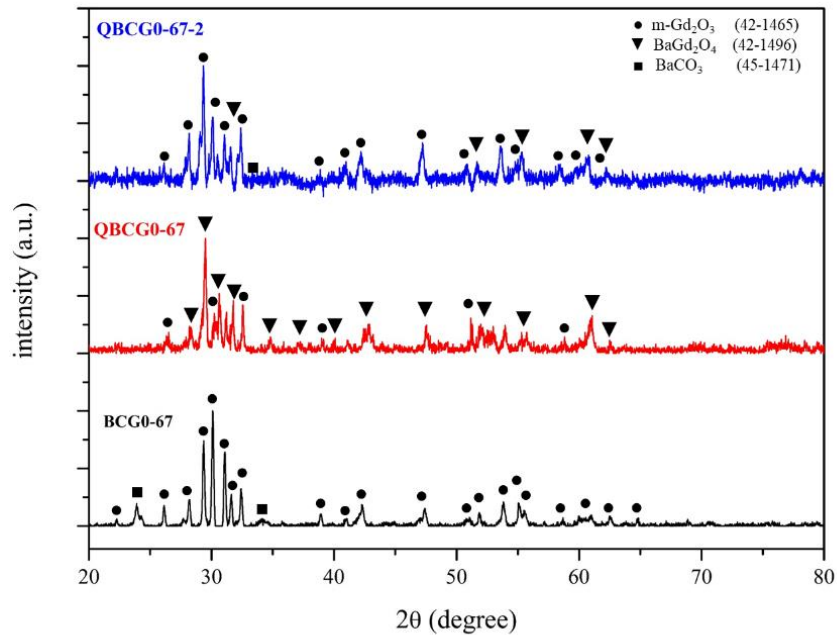


Figure 5.3 : Quenched and furnace cooled samples of BCG0-67.

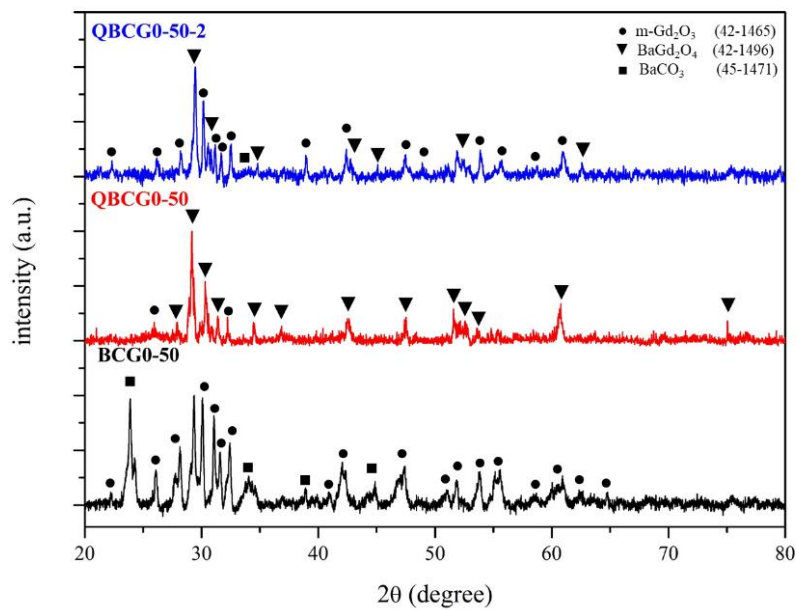
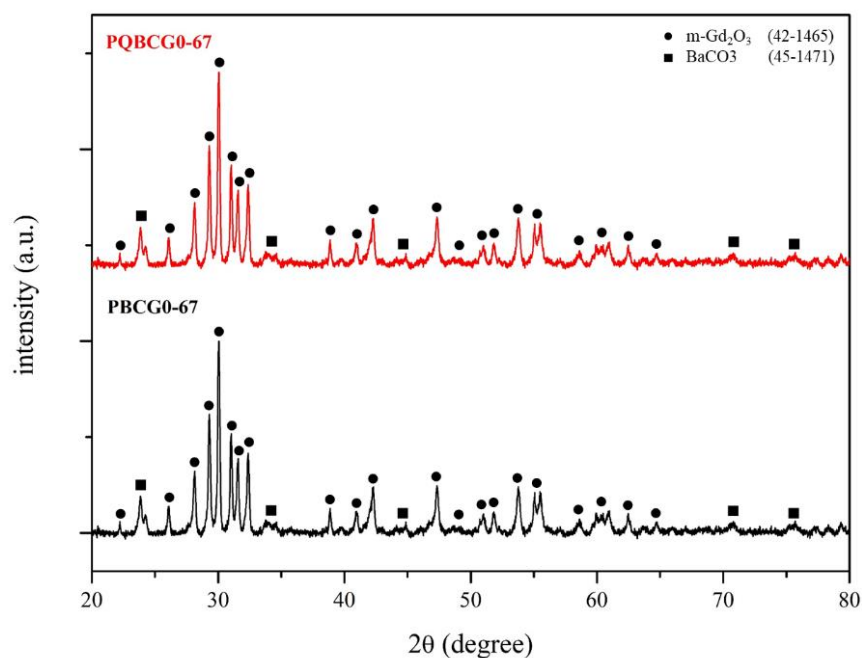


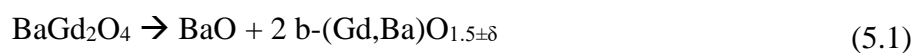
Figure 5.4 : Quenched and furnace cooled samples of BCG0-67.

BCG0-67 composition was also prepared with sol-gel method and quenched for understanding BaGd<sub>2</sub>O<sub>4</sub> phase stability. Furnace cooled and quenched samples were named as PBCG0-67 and PQBCG0-67. Quenched sample was measured with XRD after 1 week from synthesized. It was noticed that both furnace cooled and quenched samples consist BaCO<sub>3</sub> and monoclinic Gd<sub>2</sub>O<sub>3</sub> phases but quenched sample's pattern shifted to lower 2θ angles. XRD patterns of BCG0-67 can be observed in Figure 5.5. These results matched with samples which are synthesized with solid-state reaction method and they supported that BaGd<sub>2</sub>O<sub>4</sub> phase is high temperature stable phase and decomposes to BaCO<sub>3</sub> and monoclinic Gd<sub>2</sub>O<sub>3</sub>.



**Figure 5.5 :** XRD patterns of PBCG0-67 and PQBCG0-67.

According to these XRD results, BaO-GdO<sub>1.5</sub> quasi-binary phase diagram was constructed as shown in Figure 5.6. According to this phase diagram BaGd<sub>2</sub>O<sub>4</sub> phase decomposed to barium carbonate and monoclinic gadolinium oxide phases. This reaction can be observed in equation 5.1.



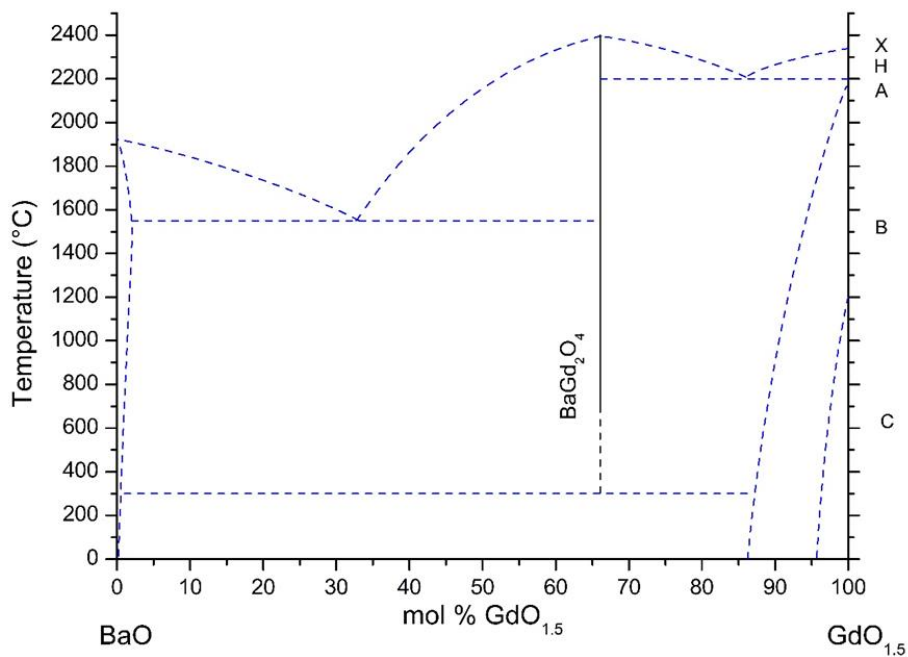


**Figure 5.6 :** BaO-GdO<sub>1.5</sub> quasi binary phase diagram.

Prepared samples can be seen in Figure 5.7. Compositions were determined according to quasi-binary phase diagrams for determination of solubility limits of the phases.

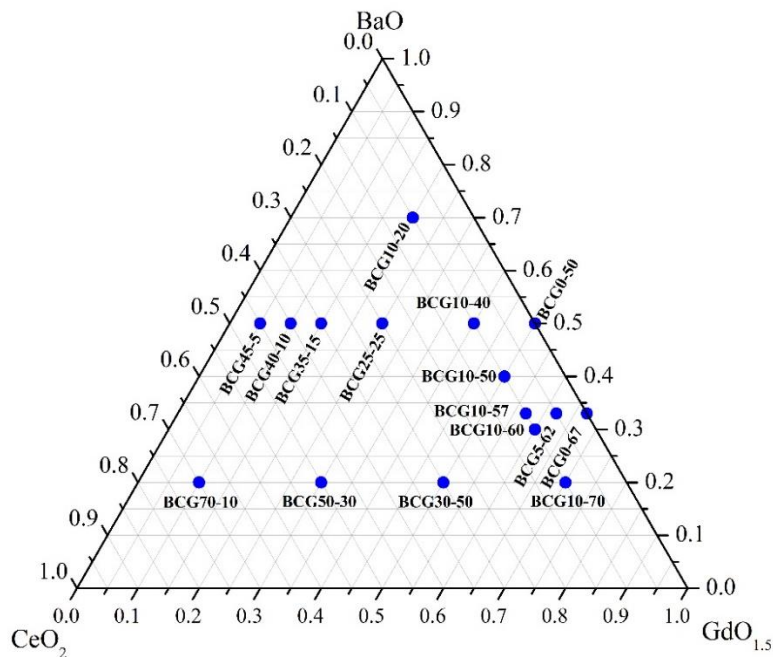


**Figure 5.7 :** Selected sample compositions.

Samples were divided into four different group and investigated each group separately. After that, XRD results of each group were compared each other thus quasi-ternary phase diagram was constructed.

First group includes BCG45-5, BCG40-10, BCG35-15 and BCG25-25. These samples were prepared for determination of solubility limit of BaCeO<sub>3</sub> phase. Figure 5.8 shows XRD results of BCG45-5, BCG40-10, BCG35-15 and BCG25-25 that were sintered at 1300°C for 48h.

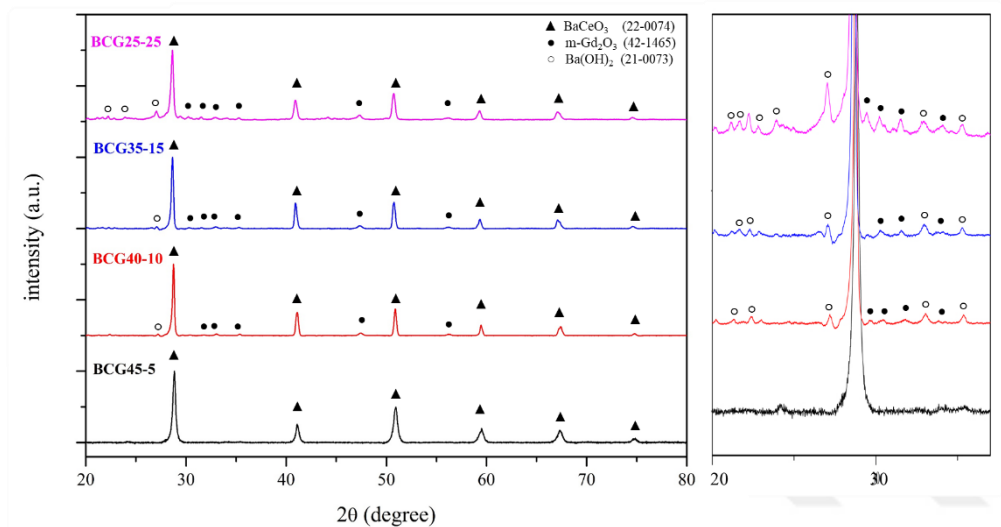


**Figure 5.8 :** XRD results of BCG45-5, BCG40-10, BCG35-15 and BCG25-25.

According to these results, BCG45-5 includes only BaCeO<sub>3</sub> or BaCe<sub>0.91</sub>Gd<sub>0.09</sub>O<sub>2.955</sub> and it is on solid solution line. Moreover, Gd-solubility limit in Ba(Ce,Gd)O<sub>3</sub> solid solution was determined as x=0.1 when compared XRD results with each other. Besides, BCG40-10, BCG35-15 and BCG25-25 include BaCeO<sub>3</sub>, monoclinic Gd<sub>2</sub>O<sub>3</sub> and Ba(OH)<sub>2</sub> phases. They contain Ba(OH)<sub>2</sub> phase because of that BaO is not stable at room temperature and it reacts with CO<sub>2</sub> and H<sub>2</sub>O forming BaCO<sub>3</sub> and/or Ba(OH)<sub>2</sub>. It has become apparent that BCG40-10, BCG35-15 and BCG25-25 are the same three-phase field. Moreover, with increasing amount of GdO<sub>1.5</sub>, *b*-type Gd<sub>2</sub>O<sub>3</sub> phase peak's intensity increased. SEM/EDS results of BCG25-25 can be observed in Figure 5.9. These results supported to XRD results and solubility limit of phases were determined by elemental analysis.

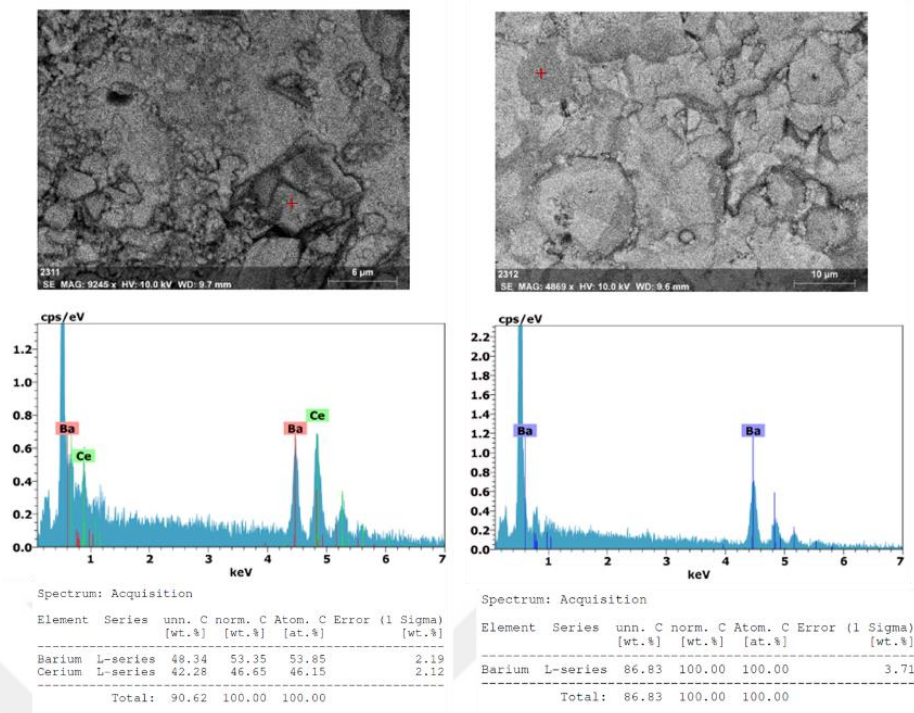


**Figure 5.9** : SEM/EDS results of BCG25-25.

In other respects, when BCG25-25 sample was sintered extra 72h at 1300°C, this sample includes *c*-type  $Gd_2O_3$  and  $BaCeO_3$  phases distinctly from 48h sample. Figure 5.10 shows 48 h and 120 h sintered samples' XRD patterns.

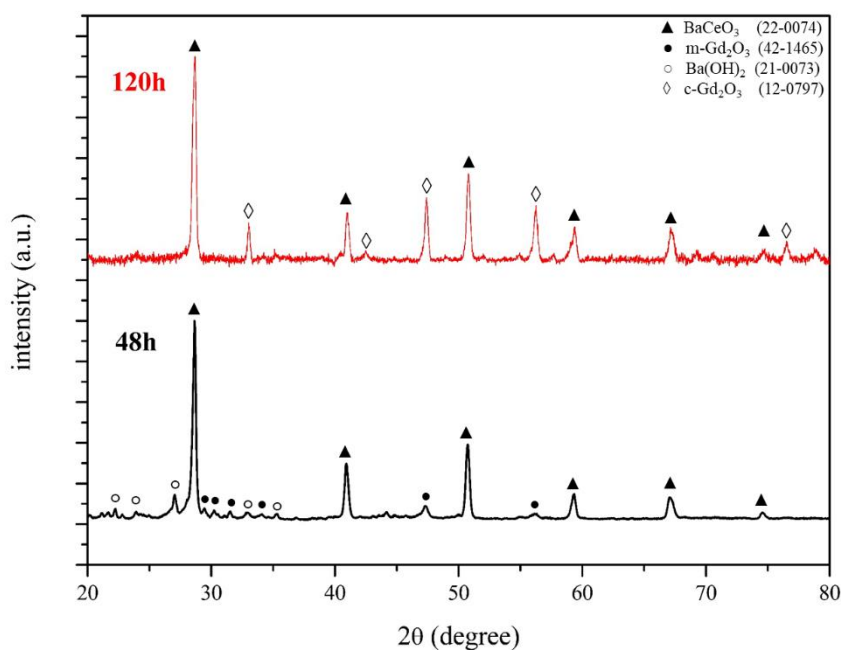


**Figure 5.10** : 48 h and 120 h sintered samples' XRD patterns.

As seen in Figure 5.10, monoclinic  $Gd_2O_3$  phase transformed to cubic  $Gd_2O_3$  phase with extra sintering. The reason of that barium amount was not sufficient for stabilizing *b*-type  $Gd_2O_3$ .

BCG70-10, BCG50-30, BCG30-50 and BCG10-70 samples XRD patterns were shown in Figure 5.11. According to this pattern, BCG70-10 includes  $BaCeO_3$  and fluorite type (*f*-type)  $CeO_2$  phases. On the other hand, with increasing amount of Gd, cubic type (*c*-type)  $Gd_2O_3$  phase could be recognized. BCG50-30 sample includes  $BaCeO_3$ , *c*-type  $Gd_2O_3$  and *f*-type  $CeO_2$ . After sample composition passed solubility limit of *f*-type ceria than only *c*-type  $Gd_2O_3$  can be seen in structure. BCG30-50 sample includes  $BaCeO_3$  and *c*-type  $Gd_2O_3$  in structure. BCG10-70 sample contains just *c*-type  $Gd_2O_3$  and it means there is an single phase solid solution field exists. The reason of that solubility limit of single phase *c*-type  $Gd_2O_3$  may be increased with sintering or cooling time. Nevertheless, BCG70-10, BCG50-30 and BCG30-50 samples are different three phase fields.

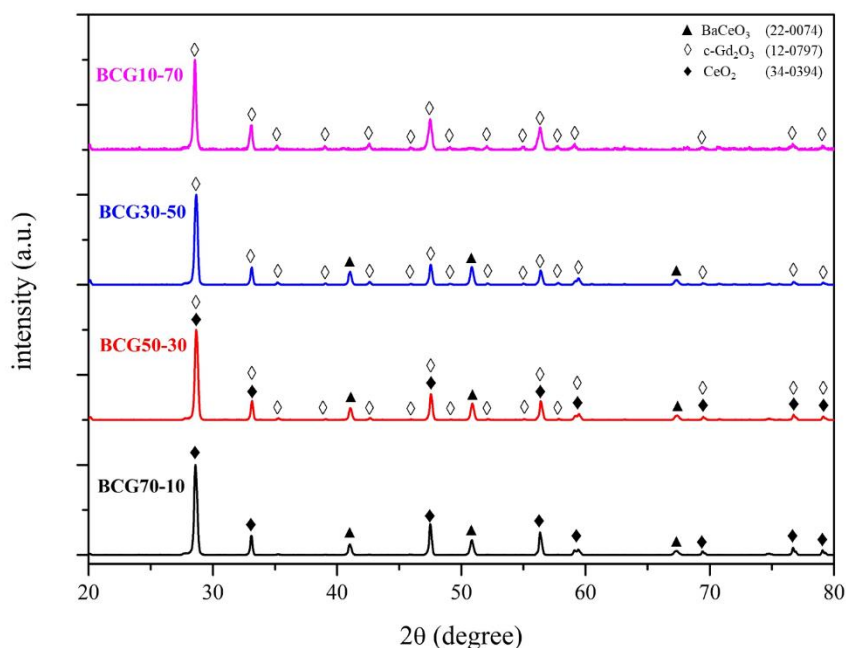


**Figure 5.11** : BCG70-10, BCG50-30, BCG30-50 and BCG10-70 samples' XRD patterns.

SEM/EDS result of BCG50-30 can be observed in Figure 5.12. According to SEM/EDS results, BCG50-30 contains  $BaCeO_3$ ,  $(Gd,Ce)_2O_3$  and  $(Ce,Gd)O_2$  phases. It was realized that small portion of Gd dissolved in Ce.

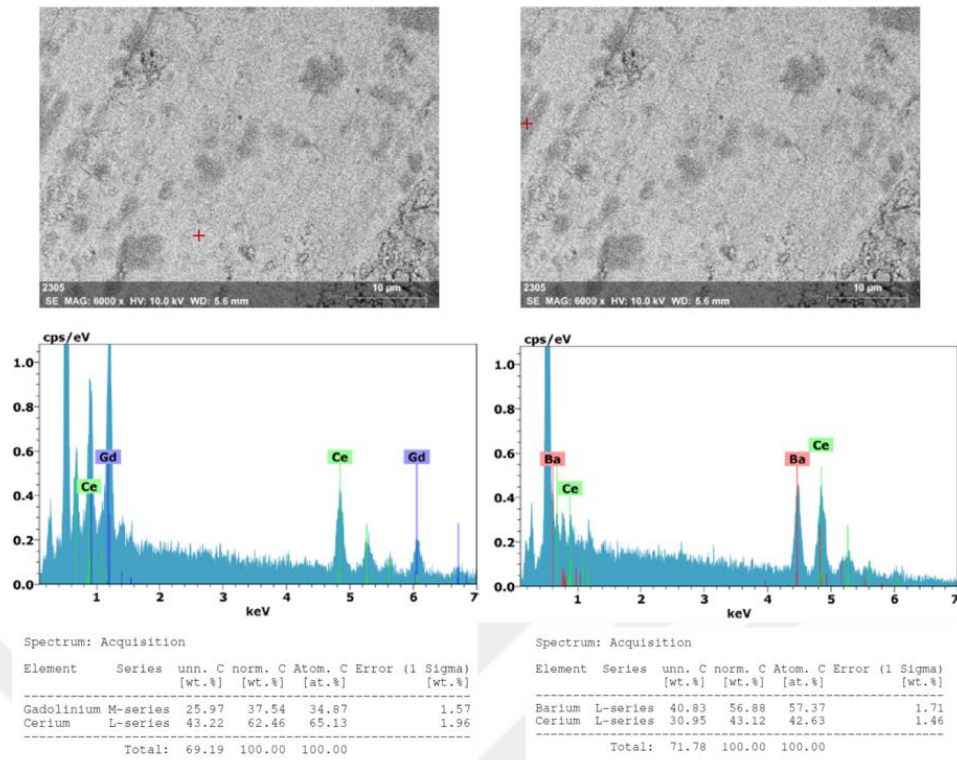


**Figure 5.12** : SEM/EDS analysis of BCG50-30.

BCG30-50 SEM/EDS result can be observed in Figure 5.13. It contains *c*-type  $Gd_2O_3$  and  $BaCeO_3$  phases.

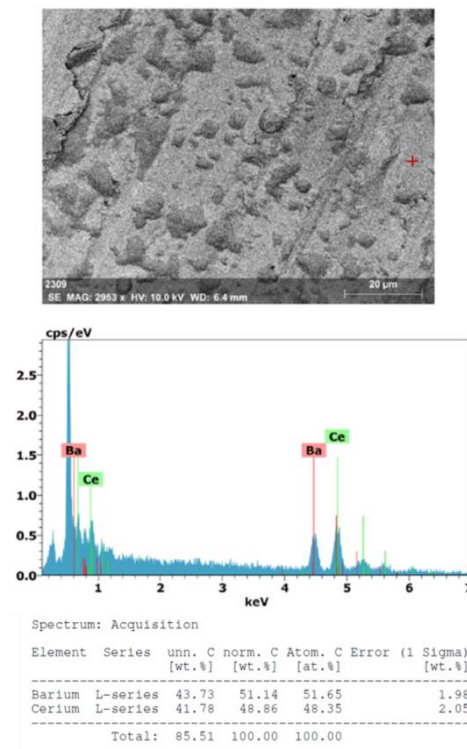


**Figure 5.13** : SEM/EDS result of BCG30-50.

Figure 5.14 shows XRD analysis of BCG10-20, it contains  $\text{BaCeO}_3$ ,  $\text{Gd}_2\text{O}_3$  and  $\text{BaO}$  but  $\text{BaO}$  is not stable at low temperature thus it had been transformed to  $\text{BaCO}_3$ . Moreover,  $\text{BaGd}_2\text{O}_4$  decomposed to *b*-type  $\text{Gd}_2\text{O}_3$  and  $\text{BaO}$ . Also *c*-type  $\text{Gd}_2\text{O}_3$  was observed because Ba amount was not sufficient for stabilizing *b*-type  $\text{Gd}_2\text{O}_3$ .

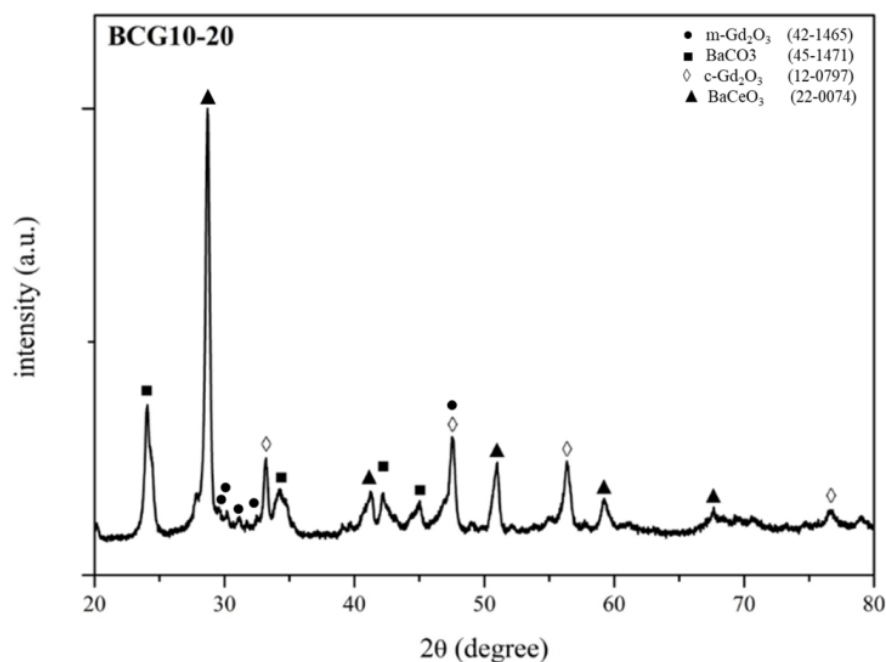


**Figure 5.14 :** A XRD analysis of BCG10-20.

According to SEM/EDS results of BCG10-20, it contains  $\text{BaO}$  and  $\text{BaCeO}_3$  phases. Figure 5.15 shows SEM/EDS results of BCG10-20. Moreover; small portion of Gd dissolved in Ba and it is another important result of this study because it was expected that Gd ions substitute Ce ions due to the fact that their ionic radius are very close each other. Furthermore, small portion of Gd ions substituted Ba ions while it dissolved cerium.

BCG10-40 48h and 120h sintered samples' XRD patterns can be seen in Figure 5.16. 48h sintered sample includes  $\text{BaCeO}_3$ ,  $\text{Ba}(\text{OH})_2$  and  $\text{BaGd}_2\text{O}_4$  phases but when it had sintered extra 72h,  $\text{BaGd}_2\text{O}_4$  decomposed to monoclinic  $\text{Gd}_2\text{O}_3$  and  $\text{BaO}$ .  $\text{BaO}$  transformed to carbonated because it is not stable at room temperature

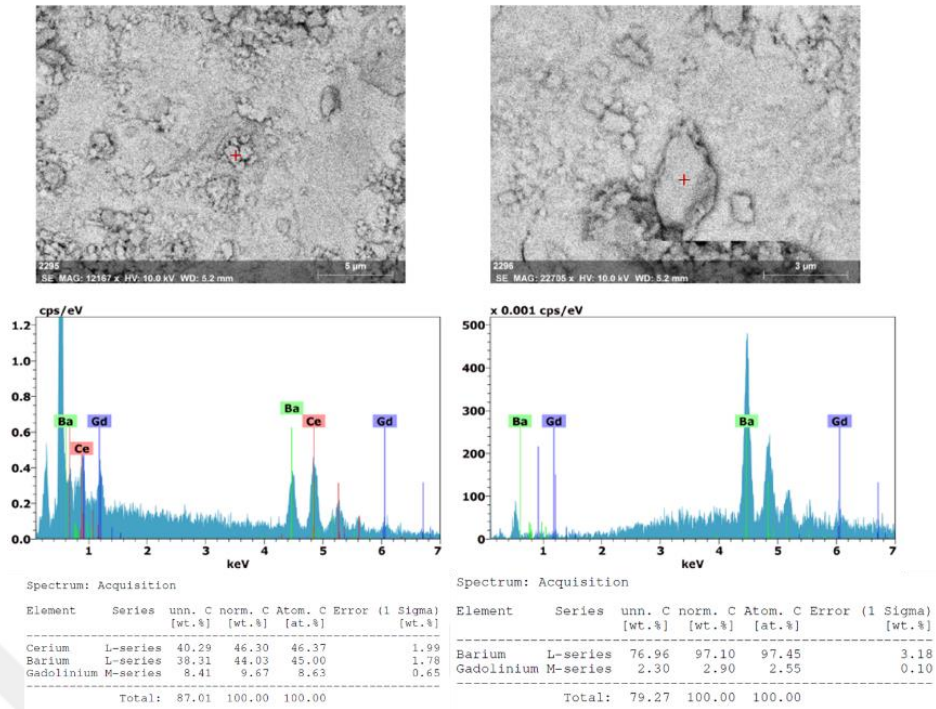


Figure 5.15 : SEM/EDS results of BCG10-20.

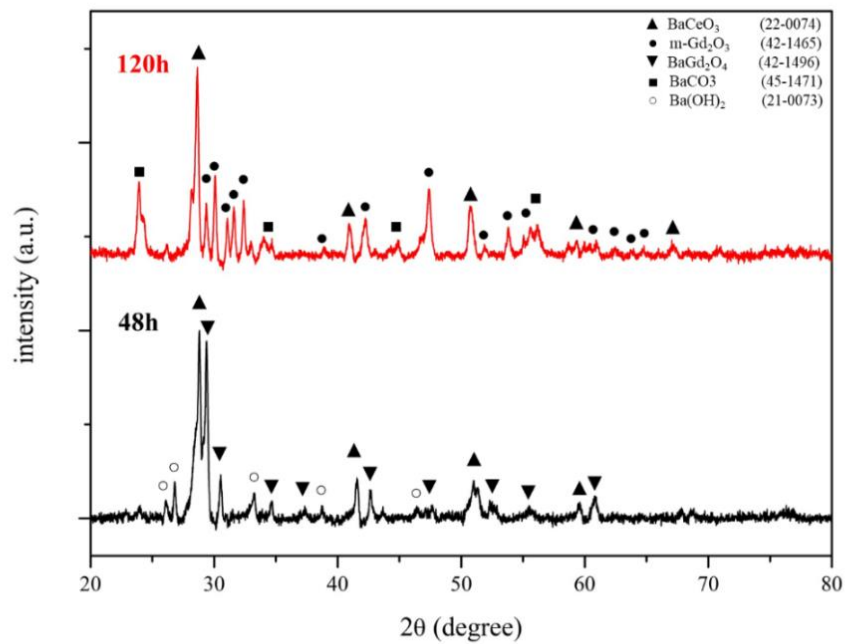
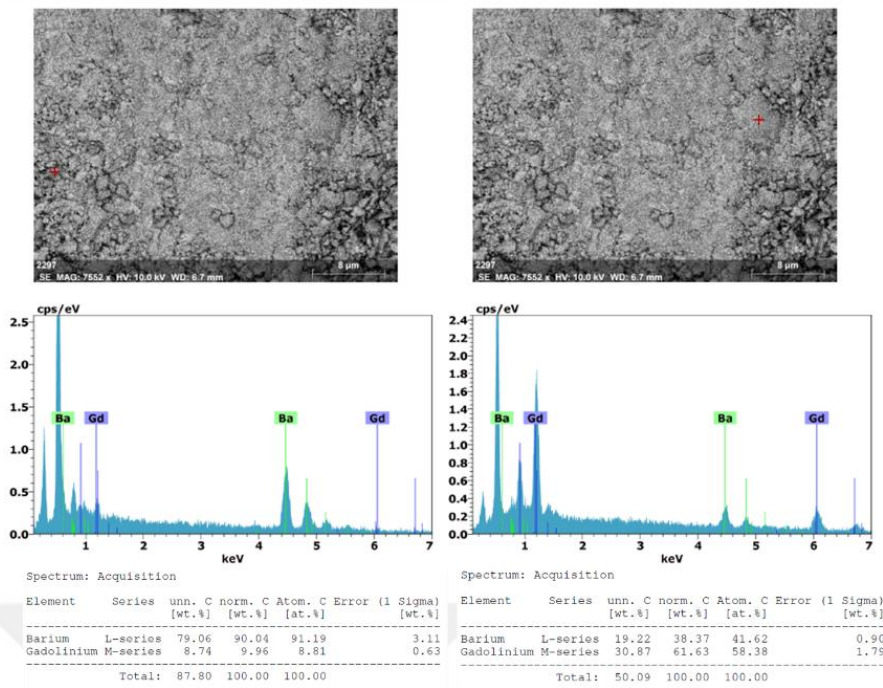


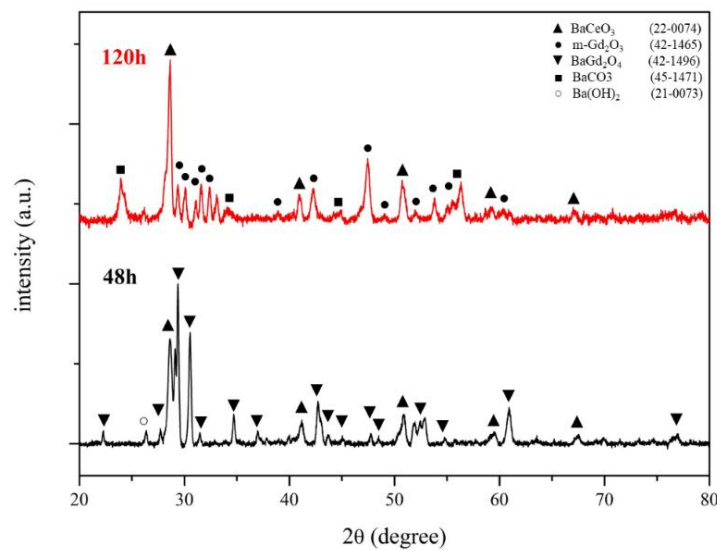
Figure 5.16 : XRD patterns of BCG10-40 with various sintering time.

SEM/EDS results of BCG10-40, which was sintered at 48 h, can be seen in Figure 5.17. SEM/EDS results matched with XRD results of 48 h sintered BCG10-40.



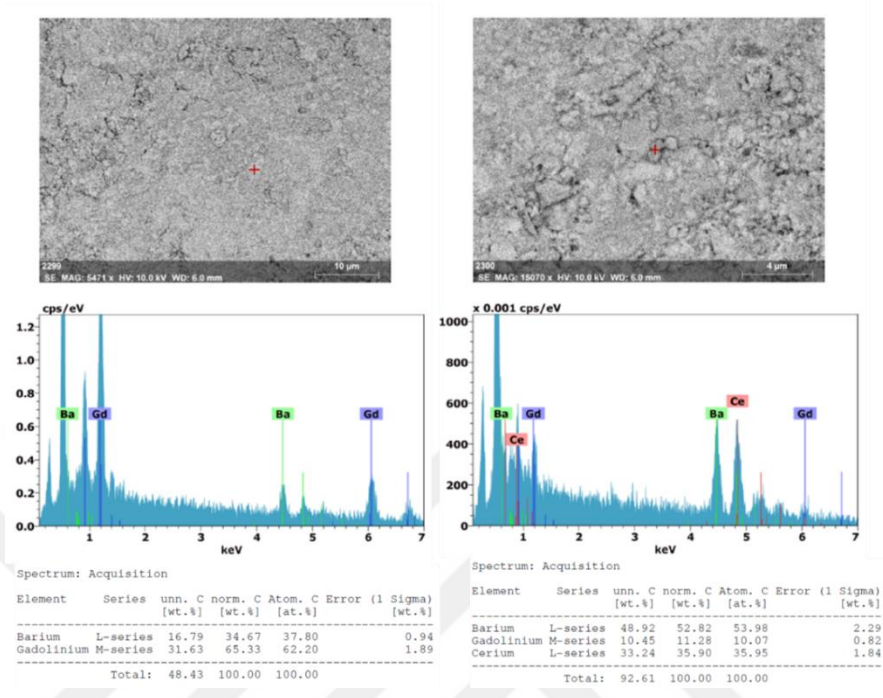
**Figure 5.17** : SEM/EDS analysis of BCG10-40.

48 h and 120 h sintered BCG10-50 samples include same phases with 48 h and 120 h sintered BCG10-40 samples. On the other hand, 120 h and 48 h sintered BCG10-40 have higher intensity  $\text{Ba}(\text{OH})_2$  phase than 120 h and 48 h sintered BCG10-50. The main reason of that BCG10-40 has higher BaO content than BCG10-50. In BCG10-50,  $\text{BaGd}_2\text{O}_4$  phase intensity higher than BCG10-40. Figure 5.18 shows XRD patterns of 48 h and 120 h sintered samples of BCG10-50.



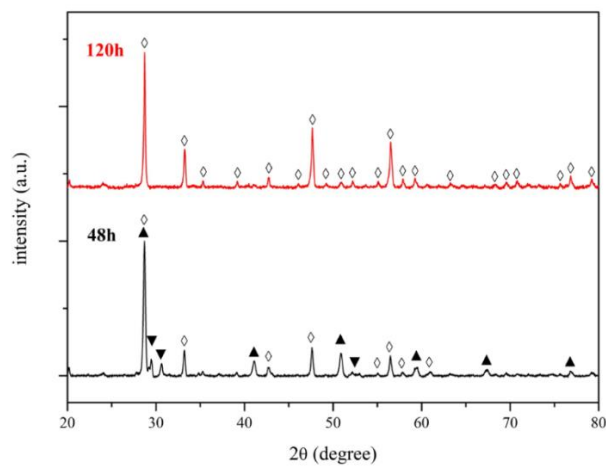
**Figure 5.18** : XRD patterns of 48 h and 120 h sintered samples of BCG10-50.

Figure 5.19 shows SEM/EDS analysis of 48 h sintered BCG10-50 sample. According to these results  $\text{BaGd}_2\text{O}_4$  phase was detected and also these results showed that Gd ions substituted to Ce ions.



**Figure 5.19** : SEM/EDS analysis of 48 h sintered BCG10-50.

When BCG10-60 sample sintered at 48h, it consists  $\text{BaGd}_2\text{O}_4$  and *c*-type  $\text{Gd}_2\text{O}_3$ . Besides, 120 h sintered sample includes only *c*-type  $\text{Gd}_2\text{O}_3$ . It shows solubility limit of *c*-type  $\text{Gd}_2\text{O}_3$  might be increased with increasing sinter time. Figure 5.20 shows XRD patterns of 48 h and 120 h sintered BCG10-60 samples.



**Figure 5.20** : XRD patterns of 48 h and 120 h sintered BCG10-60 samples.

BCG10-60 includes BaCeO<sub>3</sub> and Gd<sub>2</sub>O<sub>3</sub> phases. Figure 5.21 shows SEM/EDS results of BCG10-60. These results showed that cerium dissolved in gadolinium.

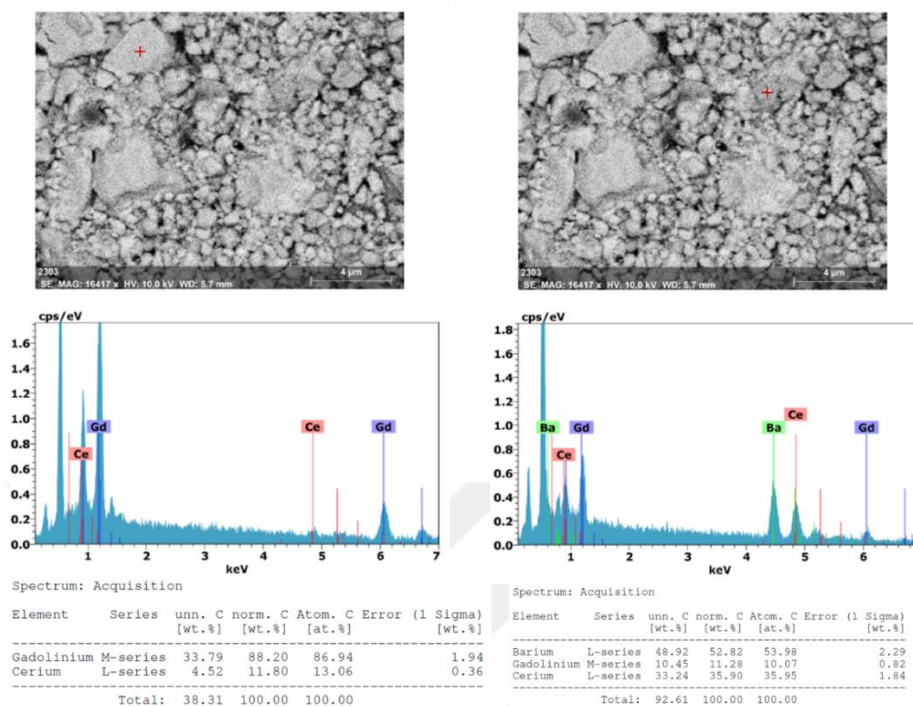


**Figure 5.21** : SEM/EDS result of BCG10-60.

XRD and SEM/EDS results of BCG10-20, BCG10-40 and BCG10-50 showed that these samples are the same three-phase field with BCG25-25, BCG35-15 and BCG40-10. Oppositely, BCG10-60 is located different three-phase field.

XRD results of BCG10-57 can be seen in Figure 5.22. Quenched sample was named as QBCG10-57. According to XRD results, quenched sample includes BaCeO<sub>3</sub>, BaGd<sub>2</sub>O<sub>4</sub> and *c*-type Gd<sub>2</sub>O<sub>3</sub>; on the other hand, furnace cooled sample consists *c*-type Gd<sub>2</sub>O<sub>3</sub>, BaCeO<sub>3</sub> and BaCO<sub>3</sub>. Moreover, comparison of quenched and furnace cooled samples demonstrated that cooling rate affects BaGd<sub>2</sub>O<sub>4</sub> phase stability. In addition, QBCG10-57 sample was measured again with XRD after almost 1 week from the first measurement and it was named as QBCG10-57-2. It has been apparent that BaGd<sub>2</sub>O<sub>4</sub> phase decomposed to BaCeO<sub>3</sub> and small portion of BaCO<sub>3</sub> at room temperature. The reason of that this phase is not stable at room temperature.

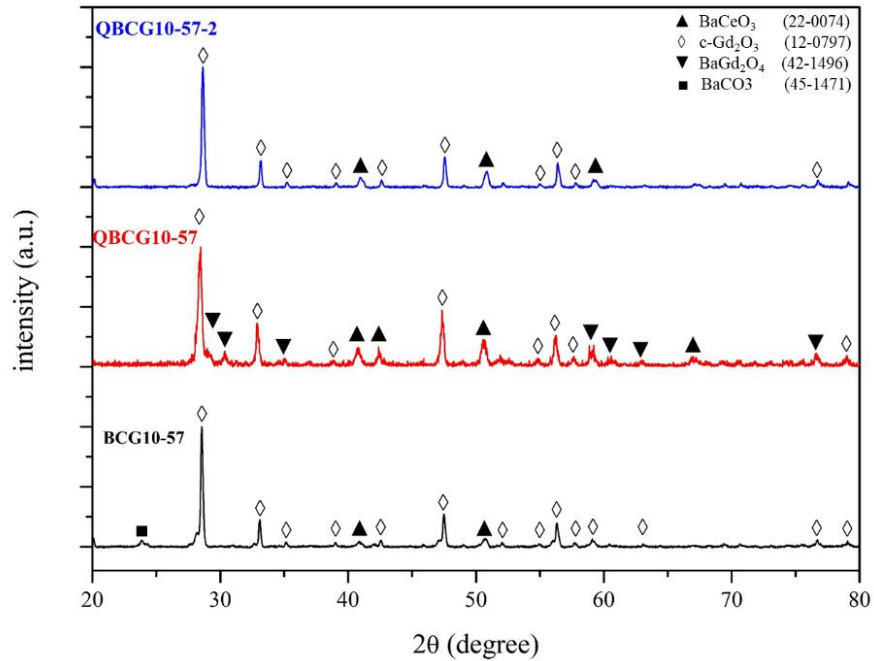


**Figure 5.22 :** Furnace cooled and quenched samples of BCG10-57.

BCG5-62 sample consists of  $\text{BaCO}_3$ , monoclinic  $\text{Gd}_2\text{O}_3$  and cubic  $\text{Gd}_2\text{O}_3$ .  $\text{BaCO}_3$  and *b*-type  $\text{Gd}_2\text{O}_3$  are product of decomposition reaction of  $\text{BaGd}_2\text{O}_4$  phase. XRD pattern of this sample can be observed in Figure 5.23.

BCG25-25 samples were prepared with sol-gel method and named as PBCG25-25. The sample, which was prepared the same composition, was quenched and named as PQBCG25-25. XRD patterns of these samples can be seen in Figure 5.24. According to XRD results, furnace cooled sample's pattern shifted to lower  $2\theta$  angles. Furthermore,  $\text{BaCO}_3$  and *c*-type  $\text{Gd}_2\text{O}_3$  did not occur in quenched sample.

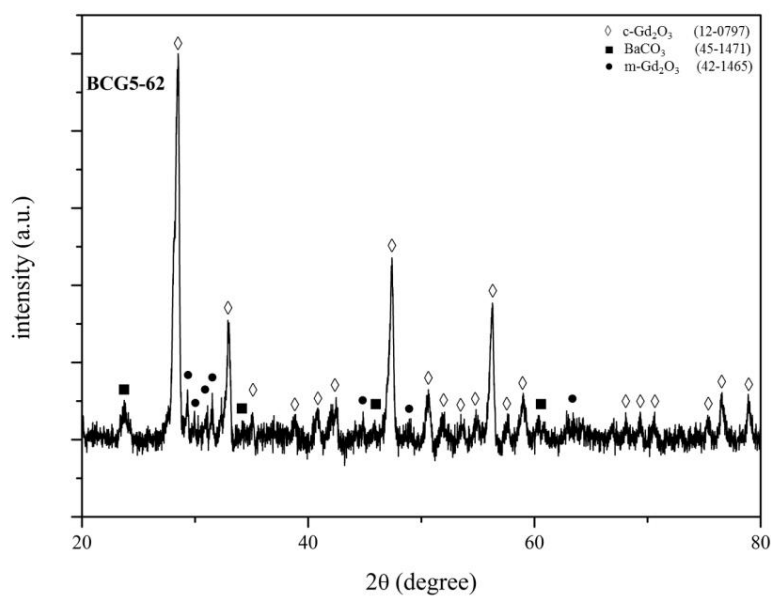


**Figure 5.23 :** XRD pattern of BCG5-62.

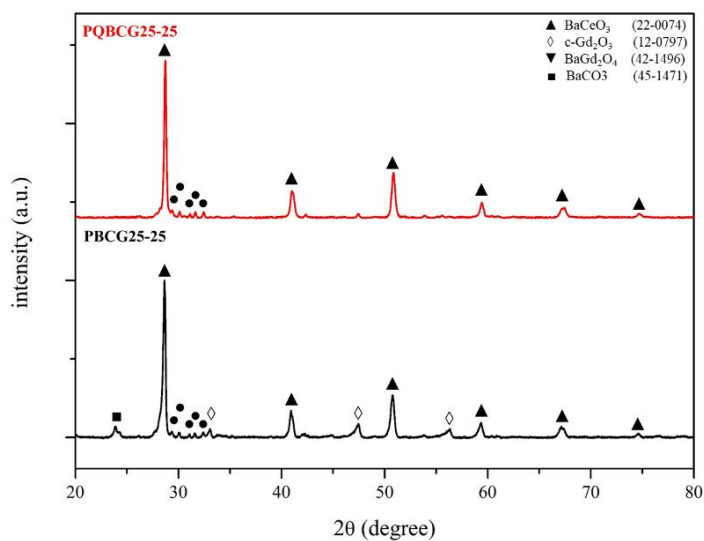


**Figure 5.24 :** XRD patterns of PBCG25-25 and PQBCG25-25.

According to XRD and SEM/EDS results BaO-CeO<sub>2</sub>-GdO<sub>1.5</sub> quasi ternary phase diagram was constructed as shown in Figure 5.25.

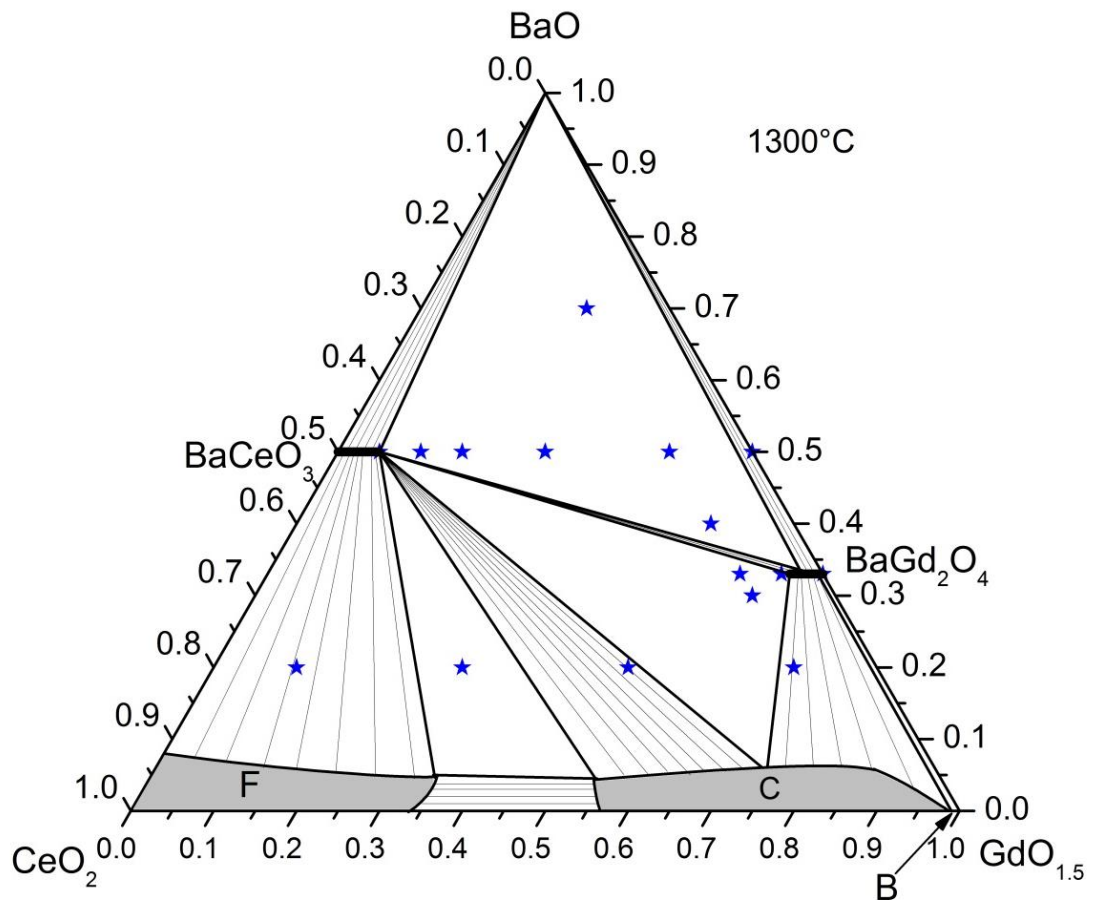


**Figure 5.25 :** BaO-CeO<sub>2</sub>-GdO<sub>1.5</sub> quasi ternary phase diagram.

An extended solubility in the Gd-doped ceria single-phase regions. The BaCeO<sub>3</sub> phase dissolved 10% GdO<sub>1.5</sub>; similarly, the BaGd<sub>2</sub>O<sub>4</sub> phase dissolves 4% Ce forming a single-phase solid solution. Besides, *f*-type CeO<sub>2</sub> solubility limit was calculated as 36% Gd and *c*-type Gd<sub>2</sub>O<sub>3</sub> solubility limit was determined between 56% and 98% Gd. Upper than 98% Gd *b*-type Gd<sub>2</sub>O<sub>3</sub> structure was observed.



## 6. CONCLUSION

Samples that include various compositions of BaO, CeO<sub>2</sub> and Gd<sub>2</sub>O<sub>3</sub> were synthesized successfully not only solid state reaction method but also sol-gel method. First of all, BaO-GdO<sub>1.5</sub> quasi binary phase diagram was examined for understanding BaGd<sub>2</sub>O<sub>4</sub> phase stability. For this purpose BCG0-67 and BCG0-50 samples were prepared solid state and sol-gel method and then quenched; moreover, quenched samples were measured again after almost one week from first measurement. It was observed that BaGd<sub>2</sub>O<sub>4</sub> phase decomposes to BaCO<sub>3</sub> and monoclinic Gd<sub>2</sub>O<sub>3</sub> phases with time. In addition, cooling rate affects this phase stability while BaGd<sub>2</sub>O<sub>4</sub> had been observed in quenched samples, it decomposed to barium carbonate and *b*-type gadolinium oxide under furnace cooling conditions. For better understanding this decomposition reaction, it is suggested to investigate the BaO-GdO<sub>1.5</sub> quasi-binary phase diagram in more details. When Gd amount increased in composition, samples cracked and mechanical strength of samples decreased with time. Also it was recognized that small amount of Gd dissolved in barium oxide.

As a result, BaO-CeO<sub>2</sub>-GdO<sub>1.5</sub> quasi ternary phase diagram was constructed at 1300°C by using various characterization methods such as XRD and SEM/EDS and synthesis methods such as conventional solid state reaction and sol-gel method.



## REFERENCES

- [1] **I. EG&G Technical Services**, “Fuel Cell Handbook,” *Fuel Cell*, vol. 7 Edition, no. November, pp. 1–352, 2004.
- [2] **X. Huang, Z. Zhang, and J. Jiang**, “Fuel Cell Technology for Distributed Generation: An Overview,” *2006 IEEE Int. Symp. Ind. Electron.*, vol. 2, pp. 1613–1618, 2006.
- [3] **N. Solak**, “Interface Stability in Solid Oxide Fuel Cells for Intermediate Temperature Applications,” Universität Stuttgart, 2007 (Doctoral dissertation).
- [4] **D. Medvedev, A. Murashkina, E. Pikalova, A. Demin, A. Podias, and P. Tsiakaras**, “BaCeO<sub>3</sub>: Materials development, properties and application,” *Prog. Mater. Sci.*, vol. 60, no. 1, pp. 72–129, 2014.
- [5] **P. Holtappels and B. R. Sudireddy**, “Ceramic Fuel Cells : Principles , Materials , and Applications,” vol. 4, 2013.
- [6] **A. Kirubakaran, S. Jain, and R. K. Nema**, “A review on fuel cell technologies and power electronic interface,” *Renew. Sustain. Energy Rev.*, vol. 13, no. 9, pp. 2430–2440, 2009.
- [7] **B. Cook**, “Introduction to Fuel Cells and Hydrogen Technology,” *Eng. Sci. Educ. J.*, vol. 11, no. 6, pp. 205–2016, 2002.
- [8] **A. B. Stambouli**, “Fuel cells: The expectations for an environmental-friendly and sustainable source of energy,” *Renew. Sustain. Energy Rev.*, vol. 15, no. 9, pp. 4507–4520, 2011.
- [9] **A. Boudghene Stambouli and E. Traversa**, “Fuel cells, an alternative to standard sources of energy,” *Renew. Sustain. Energy Rev.*, vol. 6, no. 3, pp. 297–306, 2002.
- [10] **J. M. Andújar and F. Segura**, “Fuel cells: History and updating. A walk along two centuries,” *Renew. Sustain. Energy Rev.*, vol. 13, no. 9, pp. 2309–2322, 2009.
- [11] **J. Larminie and A. Dicks**, *Fuel Cell Systems Explained*, 2nd ed. England: John Wiley & Sons Ltd., 2003.
- [12] **F. Barbir**, *PEM Fuel Cells*, Second. London: Elsevier Inc., 2013.
- [13] **B. Viswanathan and M. A. Scibioh**, *Fuel Cells: Principles and Applications*. Taylor & Francis Group, 2007.
- [14] **M. W. Ellis, M. R. Von Spakovsky, and D. J. Nelson**, “Fuel cell systems: efficient, flexible energy conversion for the 21st century,” *Proc. IEEE*, vol. 89, no. 12, pp. 1808–1818, 2001.
- [15] **V. Lawlor, S. Griesser, G. Buchinger, A. G. Olabi, S. Cordiner, and D. Meissner**, “Review of the micro-tubular solid oxide fuel cell,” *J. Power Sources*, vol. 193, no. 2, pp. 387–399, Sep. 2009.
- [16] **E. Daş, S. A. Gürsel, L. Işikel Şanlı, and A. Bayrakçeken Yurtcan**, “Thermodynamically controlled Pt deposition over graphene nanoplatelets : Effect of Pt loading on PEM fuel cell performance,” *Int. J. Hydrogen Energy*, pp. 1–11, 2017.
- [17] **A. E. Oğuz**, “Hidrojen Yakıt Pilleri ve PEM Yakıt Piliinin Analizi,” Gazi Üniversitesi, 2006 (Doctoral dissertation).

- [18] **Y. Bai, M. S. Schaberg, S. J. Hamrock, Z. Tang, G. Goenaga, A. B. Papandrew, and T. A. Zawodzinski**, “Density Measurements and Partial Molar Volume Analysis of Different Membranes for Polymer Electrolyte Membrane Fuel Cells,” *Electrochim. Acta*, vol. 242, pp. 307–314, 2017.
- [19] **T.-E. Kim, S. M. Juon, J. H. Park, Y.-G. Shul, and K. Y. Cho**, “Silicon carbide fiber-reinforced composite membrane for high-temperature and low-humidity polymer exchange membrane fuel cells,” *Int. J. Hydrogen Energy*, vol. 39, no. 29, pp. 16474–16485, 2014.
- [20] **H. Liu, C. Song, L. Zhang, J. Zhang, H. Wang, and D. P. Wilkinson**, “A review of anode catalysis in the direct methanol fuel cell,” *J. Power Sources*, vol. 155, no. 2, pp. 95–110, 2006.
- [21] **O. Z. Sharaf and M. F. Orhan**, “An overview of fuel cell technology: Fundamentals and applications,” *Renew. Sustain. Energy Rev.*, vol. 32, pp. 810–853, 2014.
- [22] **L. Carrette, K. A. Friedrich, and U. Stimming**, “Fuel Cells: Principles, Types, Fuels, and Applications,” *ChemPhysChem*, vol. 1, no. 4, pp. 162–193, 2000.
- [23] **A. Hamnett**, “Mechanism and electrocatalysis in the direct methanol fuel cell,” *Catal. Today*, vol. 38, no. 4, pp. 445–457, 1997.
- [24] **S. Wasmus and A. Küver**, “Methanol oxidation and direct methanol fuel cells: a selective review,” *J. Electroanal. Chem.*, vol. 461, no. 1–2, pp. 14–31, 1999.
- [25] **E. Gülzow**, “Alkaline Fuel Cells,” *Fuel Cell Sci. Eng.*, no. Chapter 5, pp. 97–129, 2012.
- [26] **F. Bidault, D. J. L. Brett, P. H. Middleton, and N. P. Brandon**, “Review of gas diffusion cathodes for alkaline fuel cells,” *J. Power Sources*, vol. 187, no. 1, pp. 39–48, 2009.
- [27] **G. Merle, M. Wessling, and K. Nijmeijer**, “Anion exchange membranes for alkaline fuel cells: A review,” *J. Memb. Sci.*, vol. 377, no. 1–2, pp. 1–35, 2011.
- [28] **M. Bischoff**, “Molten carbonate fuel cells: A high temperature fuel cell on the edge to commercialization,” *J. Power Sources*, vol. 160, no. 2 SPEC. ISS., pp. 842–845, 2006.
- [29] **A. L. Dicks**, “Molten carbonate fuel cells,” *Curr. Opin. Solid State Mater. Sci.*, vol. 8, no. 5, pp. 379–383, 2004.
- [30] **A. Kulkarni and S. Giddey**, “Materials issues and recent developments in molten carbonate fuel cells,” *J. Solid State Electrochem.*, vol. 16, no. 10, pp. 3123–3146, 2012.
- [31] **E. Antolini**, “The stability of molten carbonate fuel cell electrodes: A review of recent improvements,” *Appl. Energy*, vol. 88, no. 12, pp. 4274–4293, 2011.
- [32] **G. J. K. Acres**, “Recent advances in fuel cell technology and its applications,” *J. Power Sources*, vol. 100, no. 1–2, pp. 60–66, 2001.
- [33] **A. B. Stambouli and E. Traversa**, “Solid oxide fuel cells (SOFCs): A review of an environmentally clean and efficient source of energy,” *Renew. Sustain. Energy Rev.*, vol. 6, no. 5, pp. 433–455, 2002.
- [34] **S. P. S. Badwal and K. Foger**, “Solid oxide electrolyte fuel cell review,” *Ceram. Int.*, vol. 22, no. 3, pp. 257–265, 1996.
- [35] **C. Sun and U. Stimming**, “Recent anode advances in solid oxide fuel cells,” *J. Power Sources*, vol. 171, no. 2, pp. 247–260, 2007.
- [36] **R. M. Ormerod**, “Solid oxide fuel cells,” *Chem. Soc. Rev.*, vol. 32, no. 1, pp. 17–28, 2003.

- [37] **S. Singhal**, “Advances in solid oxide fuel cell technology,” *Solid State Ionics*, vol. 135, no. 1, pp. 305–313, 2000.
- [38] **A. J. Jacobson**, “Materials for solid oxide fuel cells,” *Chem. Mater.*, vol. 22, no. 3, pp. 660–674, 2010.
- [39] **J. W. Fergus**, “Electrolytes for solid oxide fuel cells,” *J. Power Sources*, vol. 162, no. 1, pp. 30–40, 2006.
- [40] **N. Mahato, A. Banerjee, A. Gupta, S. Omar, and K. Balani**, “Progress in material selection for solid oxide fuel cell technology: A review,” *Prog. Mater. Sci.*, vol. 72, pp. 141–337, 2015.
- [41] **B. C. H. Steele**, “Materials for IT-SOFC stacks - 35 years R&D: The inevitability of gradualness?,” *Solid State Ionics*, vol. 134, no. 1–2, pp. 3–20, 2000.
- [42] **M. L. Faro, S. Trocino, S. C. Zignani, and A. S. Aricò**, “4 – Solid oxide fuel cells,” in *Compendium of Hydrogen Energy*, 2016, pp. 89–114.
- [43] **J. Wu and X. Liu**, “Recent development of SOFC metallic interconnect,” *J. Mater. Sci. Technol.*, vol. 26, no. 4, pp. 293–305, 2010.
- [44] **N. Q. Minh**, “Solid oxide fuel cell technology - Features and applications,” *Solid State Ionics*, vol. 174, no. 1–4, pp. 271–277, 2004.
- [45] **J. Cao, Z. Gong, J. Hou, J. Cao, and W. Liu**, “Novel reduction-resistant Ba(Ce,Zr)<sub>1-x</sub>Gd<sub>x</sub>O<sub>3-δ</sub> electron-blocking layer for Gd<sub>0.1</sub>Ce<sub>0.9</sub>O<sub>2-δ</sub> electrolyte in IT-SOFCs,” *Ceram. Int.*, vol. 41, no. 5, pp. 6824–6830, 2015.
- [46] **K.-D. Kreuer**, “Proton Conductivity: Materials and Applications,” *Chem. Mater.*, vol. 8, no. 3, pp. 610–641, 1996.
- [47] **S. U. Dubal, C. H. Bhosale, and L. D. Jadhav**, “Performance of spray deposited Gd-doped barium cerate thin films for proton conducting SOFCs,” *Ceram. Int.*, vol. 41, no. 4, pp. 5607–5613, 2015.
- [48] **D. La Rosa, M. Lo Faro, G. Monforte, V. Antonucci, and A. S. Aricò**, “Comparison of the electrochemical properties of intermediate temperature solid oxide fuel cells based on protonic and anionic electrolytes,” *J. Appl. Electrochem.*, vol. 39, no. 4, pp. 477–483, 2009.
- [49] **R. Mukundan, P. K. Davies, and W. L. Worrell**, “Preparation and characterization of compounds in the BaBiO<sub>3</sub>–Ba(Ce<sub>1-x</sub>Gd<sub>x</sub>)O<sub>3-x/2</sub> system,” *J. Mater. Res.*, vol. 14, no. 1, pp. 124–131, Jan. 1999.
- [50] **N. Bonanos**, “Transport properties and conduction mechanism in high-temperature protonic conductors,” *Solid State Ionics*, vol. 53–56, no. PART 2, pp. 967–974, 1992.
- [51] **K. S. Knight and N. Bonanos**, “Space Group and Lattice Constants for Barium Cerate and Minor Corrections to the Crystal Structures of BaCe<sub>m</sub>Y<sub>o</sub>mO<sub>m</sub>, and BaCe<sub>0.9</sub>Gd<sub>0.1</sub>O<sub>2.95</sub>,” *J. Mater. Chem.*, vol. 4, no. 6, pp. 899–901, 1994.
- [52] **N. Bonanos**, “Ionic conductivity of gadolinium-doped barium cerate perovskites,” *Solid State Ionics*, vol. 35, no. 1–2, pp. 179–188, Aug. 1989.
- [53] **A. S. Kumar, R. Balaji, S. Jayakumar, and C. Pradeep**, “Microwave assisted sintering of gadolinium doped barium cerate electrolyte for intermediate temperature solid oxide fuel cells,” *Mater. Chem. Phys.*, vol. 182, pp. 520–525, 2016.
- [54] **N. Bonanos**, “Perovskite solid electrolytes: Structure, transport properties and fuel cell applications,” *Solid State Ionics*, vol. 79, pp. 161–170, 1995.
- [55] **N. Bonanos, B. Ellis, K. S. Knight, and M. N. Mahmood**, “Ionic conductivity of gadolinium-doped barium cerate perovskites,” *Solid State Ionics*, vol. 35, no. 1–2, pp. 179–188, 1989.

- [56] **N. Taniguchi, K. Hatoh, J. Niikura, T. Gamo, and H. Iwahara**, “Proton conductive properties of gadolinium-doped barium cerates at high temperatures,” *Solid State Ionics*, vol. 53–56, no. PART 2, pp. 998–1003, 1992.
- [57] **N. Maffei, L. Pelletier, and A. McFarlan**, “Performance characteristics of Gd-doped barium cerate-based fuel cells,” *J. Power Sources*, vol. 136, no. 1, pp. 24–29, 2004.
- [58] **A. Venkatasubramanian, P. Gopalan, and T. R. S. Prasanna**, “Synthesis and characterization of electrolytes based on BaO-CeO<sub>2</sub>-GdO<sub>1.5</sub> system for Intermediate Temperature Solid Oxide Fuel Cells,” *Int. J. Hydrogen Energy*, vol. 35, no. 10, pp. 4597–4605, 2010.
- [59] **N. Bonano, B. Ellis, and M. N. Mahmood**, “Construction and operation of fuel cells based on the solid electrolyte BaCeO<sub>3</sub>:Gd,” *Solid State Ionics*, vol. 44, no. 3–4, pp. 305–311, 1991.
- [60] **N. Taniguchi, E. Yasumoto, Y. Nakagiri, and T. Gamo**, “Sensing properties of an oxygen sensor using BaCe<sub>0.8</sub>Gd<sub>0.2</sub>O<sub>3-α</sub> ceramics as electrolytes,” *J. Electrochem. Soc.*, vol. 145, no. 5, pp. 7–11, 1998.
- [61] **D. Shima and S. M. Haile**, “The influence of cation non-stoichiometry on the properties of undoped and gadolinia-doped barium cerate,” *Solid State Ionics*, vol. 97, no. 1–4, pp. 443–455, 1997.
- [62] **C. Chen and G. Ma**, “Proton conduction in BaCe<sub>(1-x)</sub>Gd<sub>(x)</sub>O<sub>(3-α)</sub> at intermediate temperature and its application to synthesis of ammonia at atmospheric pressure,” *J. Alloys Compd.*, 2009.
- [63] **N. Taniguchi, E. Yasumoto, and T. Gamo**, “Operating Properties of Solid Oxide Fuel Cells Using BaCe<sub>0.8</sub>Gd<sub>0.2</sub>O<sub>3-α</sub> Electrolyte,” *J. Electrochem. Soc.*, vol. 143, no. 6, pp. 1886–1890, 1996.
- [64] **Y. P. Fu and C. S. Weng**, “Effect of rare-earth ions doped in BaCeO<sub>3</sub> on chemical stability, mechanical properties, and conductivity properties,” *Ceram. Int.*, vol. 40, no. 7 PART B, pp. 10793–10802, 2014.
- [65] **J. P. Guha and D. Kolar**, “Phase equilibria in the system BaO-CeO<sub>2</sub>,” *J. Mater. Sci.*, vol. 6, no. 9, pp. 1174–1177, Sep. 1971.
- [66] **Url-1** < <http://www.osakagas.co.jp/en/rd/fuelcell/sofc/sofc/system.html> >, date retrieved 20.06.2017.

## **CURRICULUM VITAE**

**Name Surname** : Çaęrı ÖZTÜRK  
**Place and Date of Birth** : Biga 13/04/1992  
**E-Mail** : ozturkcagr@itu.edu.tr

## **EDUCATION** :

- **B.Sc.** : **2015**, Istanbul Technical University, Chemical and Metallurgical Engineering Faculty, Metallurgical and Material Engineering
- **B.Sc.** : **2017**, Istanbul Technical University, Chemical and Metallurgical Engineering Faculty, Metallurgical and Material Engineering